Evaluation of Multi-Angle Imaging with Planar Organ-Targeted Positron Emission Tomography Detectors

By

Anirudh Shahi

A thesis

Presented to Lakehead University

In partial fulfillment of the requirement for the degree of

Master of Science in Physics

Thunder Bay, Ontario, Canada

Abstract

Positron Emission Tomography (PET) with 2-[fluorine-18]-fluoro-2-deoxy-D-glucose (18F-FDG) is a functional imaging modality which is capable of detecting cancer tumors based on their increased metabolic activity – a fingerprint of cancer. This capability makes PET a key tool in oncology for cancer detection. PET imaging increasingly requires the visualization of specific organs with organ-targeted PET systems in response to the clinical need to enhance the diagnostic capabilities of PET imaging.

Organ-targeted PET detectors offer improved sensitivity and spatial resolution compared to conventional whole-body (WB) PET systems. However, ring-based organ-targeted PET detectors have a fixed diameter optimized for imaging a single organ, which limits their clinical utility. In contrast, planar PET detectors, consisting of two flat panels with adjustable separation, offer greater versatility for imaging multiple organs. However, planar PET detectors have limited angular coverage, which leads to image distortion (smearing) along the axis perpendicular to the detector plane. This smearing degrades the quality of 3D reconstructed images and reduces the accuracy of activity estimation in small lesions.

The objective of this Thesis is to improve the effective angular coverage of planar PET detectors by introducing detector rotations in a method called multi-angle image acquisition and reconstruction. Experiments were conducted using the Radialis PET camera, a planar organ-targeted PET detector designed for 2D breast cancer imaging. While Radialis organ-targeted PET technology significantly improves 2D visualization of breast lesions compared to traditional WB-PET systems, its 3D imaging capabilities are limited due to insufficient angular coverage.

The experiments with simulated, standard and custom-made phantoms filled with 18F-FDG solutions demonstrated that multi-angle acquisition and reconstruction improves image quality, eliminates image artifacts and provides more accurate quantitative estimates inside the phantoms, attributable to the increased effective angular coverage.

Overall, the findings of this Thesis suggest that multi-angle imaging with planar PET detectors can achieve full 3D reconstruction, broadening the potential for multi-organ imaging with planar organ-targeted PET systems.

Acknowledgements

I would like to express my sincere gratitude to my supervisor, Dr. Alla Reznik, for providing me with the opportunity to conduct research in the exciting and meaningful field of medical imaging. Her encouragement throughout my graduate studies helped me remain optimistic, and her excellent scientific guidance has been instrumental in my growth and success as a researcher.

I would also like to thank Dr. Oleksandr Bubon for his motivation, technical insights, and engaging discussions, which helped me refine the direction of this project. Additionally, I extend my gratitude to Dr. Harutyun Poladyan for the thoughtful discussions on the physics of PET imaging and his invaluable support in my experimental work. I am also thankful to Dr. Apichart Linhananta and Dr. Tobias Preckel for taking the time to review my work and for providing valuable feedback.

I would like to acknowledge all members of Dr. Reznik's group for their wonderful camaraderie in the lab and peer mentorship. A special thanks to Alexey, János, and Kenneth for their assistance in 3D printing the phantoms that were essential for my experiments.

Finally, I am deeply grateful to my family for their unwavering and constant support in all areas of my life, which has been crucial to my success in my studies.

Table of Contents

Table of Figures

Table of Tables

List of Acronyms

PET	Positron Emission Tomography
[18F]-FDG	2-[fluorine-18]-fluoro-2-deoxy-D-glucose
WB	Whole Body
Bq	Becquerel (SI Unit)
eV	Electron Volt (SI Unit)
MeV	Mega Electron Volt (SI Unit)
keV	Kilo Electron Volt (SI Unit)
LOR	Line of Response
BGO	Bismuth Germanate
LYSO	Lutetium-Yttrium Oxyorthosilicate
GSO	Gadolinium Oxyorthosilicate
YAP	Yttrium Aluminium Perovskite
ns	Nanosecond (SI Unit)
SiPM	Silicon Photomultiplier
SPAD	Single Photon Avalanche diode
PDE	Photon detection efficiency
PMT	Photomultiplier Tube
DOI	Depth of Interaction
PVE	Partial Volume Effect
PSF	Point Spread Function
FOV	Field-of-View
AFOV	Axial Field-of-View
TFOV	Transverse Field-of-View
CT	Computed Tomography
TB	Total Body
CC	Craniocaudal
MLO	Mediolateral Oblique
MLEM	Maximum Likelihood Expectation Maximization
SM	System Matrix
LMF	List Mode File
RC	Recovery Coefficient
SOR	Spill Over Ratio

1. Introduction

1.1. Molecular Imaging

Molecular imaging is a class of non-invasive medical imaging techniques in which physiological processes can be visualized and assessed quantitatively for disease detection and treatment. During a molecular imaging scan, a patient is injected with a radiotracer designed to target a certain physiological process in the patient's body. The radiotracer distributes in the body and accumulates in targeted tissues and organs with elevated physiological processes.

Molecular imaging is becoming increasingly important in the realm of personalized or precision medicine with the requirements to deliver "the right treatment to the right patient at the right time" since it can provide detailed molecular and functional information not available with anatomical medical imaging, and as such, detect medical conditions more accurately.

Positron Emission Tomography (PET) stands out as a highly sensitivity molecular imaging technique primarily used in oncology to visualize increased metabolic processes within cancerous tissues. PET radiotracers decay primarily through positron emission and it ultimately leads to two antiparallel gamma rays with a distinct energy of 511 keV. The goal of a PET camera is to detect these gamma rays emerging from the patient's body and create a spatial distribution of the injected radiotracer which reflects the underlying pathology.

1.2. Physics of PET

1.2.1. Positron Emission and Annihilation

1.2.2. Radioactive Decay

The radiotracers used in PET are molecules that have been labeled with a radionuclide, which is an atom with an unstable nucleus due to an excess number of protons or neutrons. A radionuclide will undergo radioactive decay which leads to a change in the number of protons or neutrons and allows the nucleus to reach a more energetically favored state. The mode of radioactive decay depends on the ratio of neutrons and protons inside the nucleus. Proton-rich nuclei decay by converting a proton into a neutron and a positron to conserve charge, Eq. 1.

$p \rightarrow n + e^{+} + v$	*1*

Positrons are anti-particles of electrons, meaning that they have the same mass as an electron but a charge of the same magnitude but opposite sign of an electron. The radionuclides used in PET are proton-rich and, therefore, the decay results in the emission of a positron and the conversion of the radionuclide into a stable nuclide with the proton converted to a neutron. The nuclear decay can be represented as follows, Eq. 2:

$${}^{A}_{Z}X \rightarrow {}_{Z-1}{}^{A}Y + e^{+} + v$$	*2*

Here, Z is the number of protons, X and Y are the symbols for the elements with atomic number Z and Z-1, respectively, and A is the total number of nucleons. Note, β^{+} decay reduces the atomic number by one so that the daughter atom has an excessive electron. So, an orbital electron is emitted in the process to form a neutral atom, ${}_{Z-1}{}^{A}Y$, and to reach its ground state.

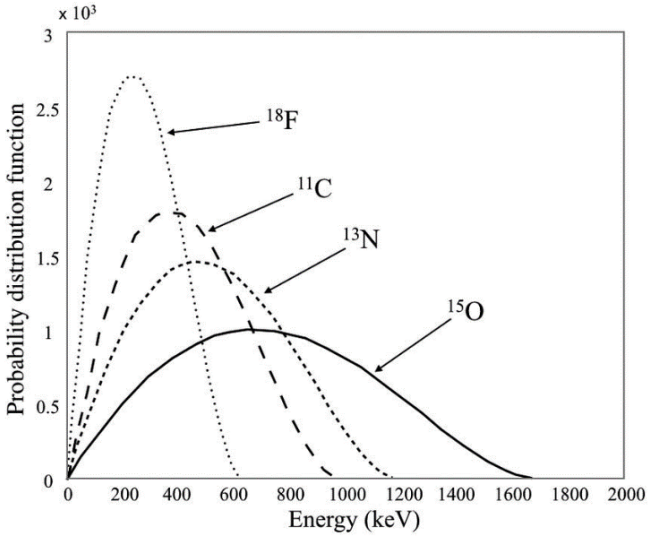

Figure 1. Spectrum of possible kinetic energies from positron emitting radionuclides commonly used in PET imaging. Source: image adopted from Del Guerra et al.[1]

The net energy released in positron emission, and the momentum, is shared between the daughter nucleus, positron, and neutrino. The positron is emitted with a distribution of kinetic energies up to a maximum endpoint energy, E_{max}, as shown in Figure 1. The maximum kinetic energy of the positron is determined by the difference in the atomic masses of the parent atom and daughter atom, taking into account gamma-ray emissions that may occur if the transition is not between

the ground states of the two nuclei. At the low end of the spectrum in Figure 1, all the energy released during the nuclear reaction is transferred to the antineutrino and the momentum is conserved by the small recoil of the daughter nucleus. The maximum endpoint energy represents maximum energy transfer to the positron and the neutrino's energy approaches zero. The mean kinetic energy of the emitted positrons is $0.33 \times {E_{max}}^2$.

Proton-rich nuclei may also decay via electron capture in which the nucleus absorbs an orbital electron from the inner K or L shells, converting a proton into a neutron and releases a neutrino, Eq. 3. Electron capture results in the same daughter nucleus as in positron emission. However, the filling of the vacancy left by the captured orbital electron results in the emission of characteristic x-rays. Positron emission and electron capture are competing processes, with positron emission usually being the dominant mode of decay in low Z nuclei, and electron capture being dominant in high Z nuclei.

$p + e^- \rightarrow n + v$	*3*

Although the spontaneous decay of a given unstable nuclei is random, a sample of identical radioactive atoms decays exponentially and each sample has a characteristic half-life, which is the time required for half of the atoms in the sample to decay. In fact, the radioactivity A of a sample at time t can be determined using the half-life $T_{1/2}$, initial radioactivity at some reference time t = 0, and an exponentially decaying function:

$A(t) = A(0) \times \exp\left(-ln2 \times t/T_{1/2}\right)$	*4*

The radioactivity is defined as the number of disintegrations per second and is measured in units called bequerel (Bq):

$1 \text{ bequerel (Bq)} = 1 \text{ disintegration per second}$	*5*

Table 1 summarizes the unique characteristics associated with the radioactive decay of commonly used positron-emitting radionuclides in PET imaging. Most of the shown radionuclides have a half-life of less than two hours.

Table 1. Half-life, maximum kinetic energy of the emitted positrons, and the positron emission branching fraction for commonly used radionuclides in PET imaging. Source: table adopted from Conti et al.[3]

Radionuclide	Half-life	Emax (MeV)	Emean (MeV)	$\beta^{+} Branching\ Fraction$
11C	20.4 min	0.960	0.386	1.00
13N	9.97 min	1.199	0.492	1.00
15O	122 s	1.732	0.735	1.00
18F	109.8 min	0.634	0.250	0.97

1.2.2.1. Positron Range

Upon emission, the positrons will interact with atomic electrons and nuclei through the Coulomb force, losing energy in a stochastic fashion and slowing down[4]. The positrons primarily lose energy via inelastic collisions with atomic electrons and less commonly undergo elastic collisions with atomic nuclei. The positron typically undergoes a large number of collisions, losing a substantial kinetic energy in the process until the particle is completely or almost completely stopped. The energy deposited per unit length rapidly increases as the positron slows down and, therefore, most of the energy deposited along its track will be near the end[4].

Table 2. Positron range, in water, of commonly used radionuclides in PET imaging. Source: table adopted from Conti et al.[3]

Radionuclide	Half-life	Maximum Range (mm)	Mean Range (mm)
11C	20.4 min	4.2	1.2
13N	9.97 min	5.5	1.8
15O	122 s	8.4	3.0
18F	109.8 min	2.4	0.6

The positron range is defined as the maximum distance it penetrates, for all possible beta decay energies, before it loses all its kinetic energy and stops. It should be noted that the positron range is less than the total path travelled by the positron. The positron range associated with a given radionuclide depends on the mean kinetic energy of the emitted positron, as shown in Table 2; positrons emitted with higher mean kinetic energies will lose energy at a lower rate and travel further from their starting position before stopping. Additionally, high-atomic-number, high-density materials will have the greatest stopping power and lead to a shorter positron range. The values shown in Table 2 are for positron range in water but the values are smaller in bones and much larger in the lungs which contain air.

As discussed in the subsequent section, PET detectors estimate the site of positron-electron annihilation and not positron emission. Therefore, positron range causes mispositioning of the radiotracer location since the positron moves away from the site of emission before annihilating with an electron, Figure 2.

1.2.2.2. Positron-Electron Annihilation

After losing sufficient energy, the positron will interact with an electron and form a hydrogen-like state called a positronium. The positronium lasts for a short time before a process called annihilation occurs, during which the mass of the two particles is converted into electromagnetic energy in the form of two simultaneously generated photons, Figure 2.

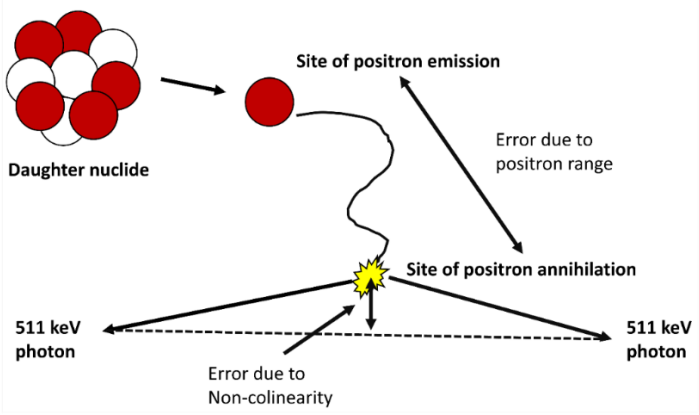

Figure 2. Mispositioning error arising from positron range and noncollinearity of the annihilation photons.

The positron and electron are almost at rest when annihilation occurs and have an almost net-zero momentum. So, two photons are emitted in opposite directions, ~180° apart, with combined energy equal to the rest mass of the electron and the positron, to ensure conservation of momentum and energy. This equation can be used to calculate the total energy of the photons:

$E = mc^2 = m_e c^2 + m_p c^2$	*6*

Where m_e is the mass of the electron and m_p is the mass of the positron and c is the speed of light. The combined energy of the annihilation photons is 1.022 MeV and individual energies of 0.511 MeV (or 511 keV). The annihilation photons are sometimes referred to as gamma rays because their energy falls within the gamma ray region of the electromagnetic spectrum and have properties identical to gamma rays. Strictly speaking, however, gamma rays refer to radiation that originates directly from the nucleus following radioactive decay. The annihilation photons are then absorbed by a pair of PET detectors which are responsible for determining the distribution of the injected radiotracers.

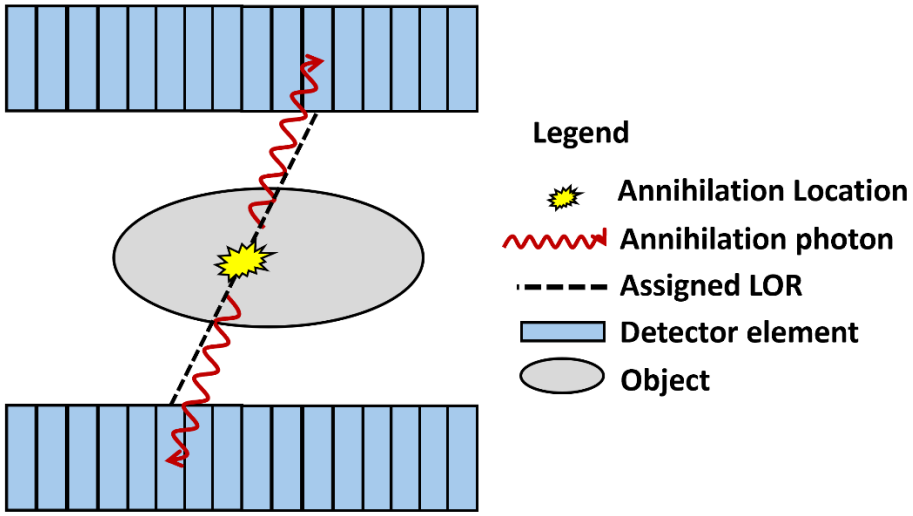

Figure 3. Line of response, indicated by the dashed line, which is formed by a line connecting a pair of detectors which absorbed the annihilation photons.

Because all annihilation photons are emitted ~180° apart, the line joining the photons will intersect the location of annihilation. PET detectors use this geometric relationship to create a

line, called the line of response (LOR), which connects the pair of detectors which absorbed the annihilation photons, Figure 3. The LOR can be used to give an indication (within a line, or more accurately, within a volume) of where the annihilation occurred. Generally, millions of LORs are used in determining the distribution of radiotracers inside the body.

However, since the electron and positron are, generally, not at rest during the annihilation, there will be a non-zero net momentum and the annihilation photons will not be exactly 180° apart; that is, the photons do not travel along a colinear path. The annihilation photons will actually be emitted with a distribution of angles around 180°. As with the positron range, the noncolinearity introduces blurring in PET images since the LOR calculated by the detectors will not pass through the location of annihilation, see Figure 2. The noncolinearity is independent of the radionuclide, and thus the initial energy, since the positrons must lose most of their kinetic energy before they annihilate. The positional error, Δ_{nc}, resulting from noncolinearity depends on the diameter of the PET detector, D, see Eq. 7, which means that increasing the diameter of the detector leads to a larger error[2]:

$\Delta_{\mathrm{nc}} = 0.0022 \times D$	*7*

Together, the positron range and noncolinearity place finite limits on the spatial resolution attainable with PET and result in blurring of the reconstruction images.

1.2.3. Gamma-ray interactions

In this section, we discuss the photon interactions with matter in the surrounding tissues and the PET detectors through the photoelectric effect and Compton scattering.

1.2.3.1. Photoelectric effect

The photoelectric effect refers to the process in which an incident photon is completely absorbed by a bound electron. The process typically involves absorption of a photon by tightly bound electrons in an inner orbital shell (K, L, M-shells). The photon's energy is transferred into the binding energy and kinetic energies of the ejected electron and the recoiling atom. The kinetic energy of the atom is significantly smaller than the kinetic energy of the electron, E_e, which can

be calculated using the difference between the energy of the photon, E_γ, and the electron's binding energy, E_B.

$E_e = E_\gamma - E_B$	*8*

This equation shows that the photon cannot undergo photoelectric absorption by an electron with a binding energy greater than the energy of the photon, $E_B > E_\gamma$. Photons with energy less than the binding energy of a K-shell electron will instead undergo photoelectric absorption with L or M-shell electrons. However, if the photon energy exceeds the binding energy of the K-shell electron, it will selectively interact photoelectrically with K-shell electrons[5]. The vacancy created after the ejection of the photoelectron is filled by cascading electrons from outer shells, resulting in the emission of characteristic X-rays, a few keV, and Auger electrons. The emitted X-rays and the electrons are quickly absorbed in the medium in the vicinity of the site of emission.

The probability of a photon undergoing photoelectric absorption per unit distance strongly depends on the atomic number Z. Figure 4 shows the dominant mode of interaction depending on the atomic number, Z, of the material and the photon energy. Generally, photoelectric effect is dominant for relatively low energies of photons and Compton scattering becomes dominant for larger energies. For the energies relevant in PET imaging (0.511 MeV), the photoelectric effect becomes dominant as the effective atomic number of the absorbing material increases, Figure 4. The probability of a photon undergoing photoelectric absorption is roughly given by Z^5/E_γ^3[6]. During photoelectric absorption, energy from the gamma rays is deposited in a localized area. This leads to improved accuracy in energy and position calculation compared to Compton scattering which involves multiple interactions in a detector and only partial energy may be deposited in the detector. For this reason, high atomic number and high density are used in PET detectors to optimize the probability for the complete photoelectric absorption of the gamma rays.

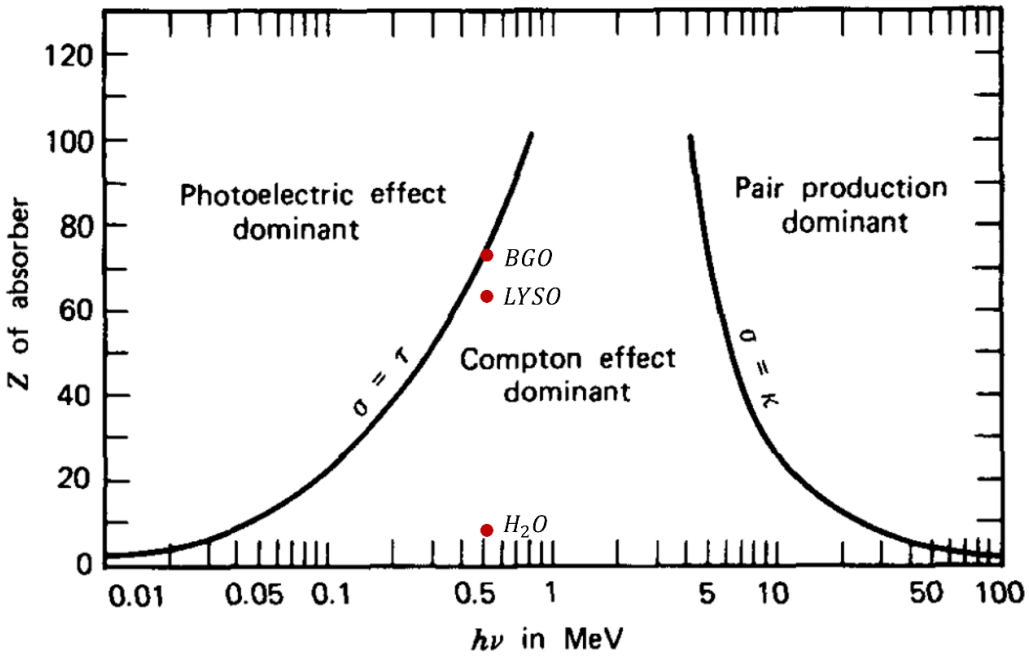

Figure 4. Dominant interaction processess of X-rays and gamma-rays depending on the incident photon energy and atomic number, Z, of the material. Here, τ, σ, κ represent the probability of interaction via the photoelectric effect, Compton scattering, and pair production, respectively. The dominant interactions have been marked for a 0.511 MeV photon interacting in BGO, LYSO, and water with effective atomic numbers of 73, 64, and 7.42, respectively. Source: image adapted from Cherry et al., 2012.[7]

1.2.3.2. Compton scatter

Compton scattering occurs when a photon scatters off a free or a loosely bound electron (in the outer-atomic-shell), transferring some of its energy to the electron and changing direction. The recoil electron is absorbed within a few millimeters depending on the absorbing material and its initial energy. Using conservation of momentum and energy we can find a relationship between the initial energy of the photon, E, and the energy of the scatter photon E_{sc} and the scattering angle, θ.

$$E_{sc} = \frac{m_e c^2}{\frac{m_e c^2}{E} + 1 - cos\theta} \quad (9)$$

In this relation, m_e is the rest mass of the electron. The energy transferred to the electron, E_{re}, is equal to the difference between the initial energy of the photon and the scatter photon $E - E_{sc}$, which is given by:

$$E_{re} = E - E_{sc} = E \times \frac{(1 - cos\theta)}{\left(\frac{m_e c^2}{E} + 1 - cos\theta\right)} \quad (10)$$

The final photon energy falls off smoothly with increasing scattering angle and it corresponds to a more energetic recoil electron. The relationship in Eq. 10 shows that maximum energy transfer occurs when $\theta = 180°$ and, in this case, the photon is backscattered. The maximum energy transferred to the electron is given by (with the initial E energy set to 511 keV):

$$E_{max} = \frac{2(511\ keV)^2}{2(511\ keV) + m_e c^2} = 340\ keV \quad (11)$$

This value is the maximum recoil electron energy (minimum scatter for the photon energy) and produces the so-called Compton edge in the energy spectrum to the left of the 511 keV photopeak. The probability of Compton scatter as a function of scatter angle is given by the Klein-Nischina equation and the angular distribution of the scattered photons is plotted for various energies in Figure 5. As shown, annihilation photons with energies of 511 keV undergo mainly small-angle forward scatter. Furthermore, the probability of Compton scattering per unit length in a medium is linearly proportional to the atomic number of the medium.

Figure 4 shows that Compton scattering is the dominant interaction process for 511 keV photons in both water and high effective atomic number materials used in scintillators, such as LYSO and BGO. Compton scattering contributes to the mispositioning of the LOR because the photons deviate from traveling along a straight line, causing the LORs joining these photons to not intersect at the annihilation location. Consequently, PET detectors use a lower energy discriminator to eliminate photons that have undergone high-angle Compton scattering and minimize image blur caused by scatter.

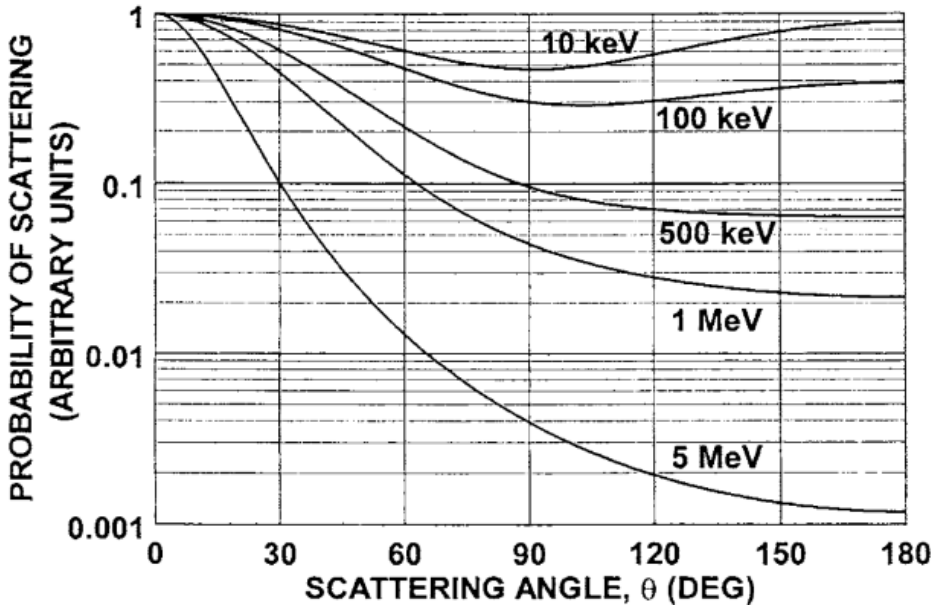

Figure 5. Relative probability of Compton scattering versus scattering angle. Source: image adopted from Cherry et al., 2006.

1.2.3.3. Attenuation of Gamma-Rays

A parameter called the linear attenuation coefficient μ is used to represent the probability per unit distance that an interaction will occur between the photon and the medium. The attenuation coefficient is directly related to the total interaction cross section and depends on the photon energy, atomic number, and density of the surrounding material. The attenuation of the 511 keV annihilation photons in matter typically involves photoelectric absorption or Compton scattering and the attenuation coefficient consists of contributions from these two types of interactions:

$\mu \approx \mu_{compton} + \mu_{photoelectric}$	*12*

The attenuation of a photon beam in a medium follows an exponential function

$I = I_0 e^{-\mu x}$	*13*

where I is the number of photons that travelled straight through the material without any interactions, I_0 is the number of photons in the initial beam of photons, and x is the penetration depth. The attenuation coefficients for 511 keV photons are shown in Table 3 for different materials encountered in PET imaging. The attenuation coefficient is higher for Compton scatter in soft tissues and hard tissues, such as bone compared to the attenuation coefficient for photoelectric effect. Depending on the site of annihilation, the photons may traverse several centimeters before exiting the patient's body. Table 3 shows that the radiation is reduced by half after traversing 7.2 cm of soft tissue and 4.1 cm of hard tissue. This indicates that there is significant attenuation within the patient's body, mainly due to Compton scattering. So, PET detectors typically use mathematical algorithms to remove apparent background activity due to attenuation of the gamma rays.

Table 3 also provides the attenuation coefficient for BGO, which is one of the common scintillators used in PET detectors. Scintillators are used in PET detectors to absorb the annihilation photons and, therefore, a high attenuation coefficient is desired when choosing the scintillating material to maximize photon detection. Scintillators with a higher cross section for photoelectric absorption and a lower cross section for Compton scatter are preferable for optimal positioning and energy calculation accuracy. BGO has a relatively high attenuation coefficient, and photoelectric absorption is the dominant mode of interaction for 511 keV photons. However, cerium-doped lutetium-yttrium oxyorthosilicate (LYSO:Ce) is more commonly employed in modern PET detectors because it has more desirable scintillating properties which will be discussed later. Finally, Table 3 provides the attenuation coefficients for lead and tungsten which are highly attenuating materials and are primarily used for shielding. As evident by the half-value thickness, a few centimeters of these materials are usually used for absorbing incoming radiation and minimizing radiation exposure to the clinicians and patients.

Table 3. Compton scatter, photoelectric absorption, and total linear attenuation coefficients for different materials at 511 keV. The half-value thickness indicates the thickness of material which reduces the intensity of the incident beam of radiation by half its value. Source: image adopted from Cherry et al.[2]

Material	$\mu_{Compton}(cm^{-1})$	$\mu_{photoelectric}(cm^{-1})$	$\mu(cm^{-1})$	Half-value thickness (cm)
Soft tissue	0.096	0.00002	0.096	7.2
Bone	0.169	0.001	0.17	4.1
Bismuth Germanate (BGO)	0.51	0.40	0.96	0.76
Lead	0.76	0.89	1.78	0.42
Tungsten	1.31	1.09	2.59	0.29

1.3. Basics of PET Detection

The following section describes the two major components of a PET detector: a scintillator and a photosensor, which absorbs gamma rays and generate an electrical signal proportional to the amount of energy deposited by the photon (Figure 6). The signals from all photosensors can be summed to calculate the energy deposited in the detectors. Additionally, these signals can be used in a weighted sum along with the corresponding photosensor positions to determine the coordinates of interactions.

1.3.1. Scintillators

PET detectors use an indirect conversion mechanism of the annihilation photons into measurable electrical signal. The indirect conversion begins with scintillators, which are transparent materials and emit light in the visible part of the electromagnetic spectrum when excited by high-energy particles or photons. The light is emitted isotropically and the amount of photons produced is proportional to the energy deposited in the material.

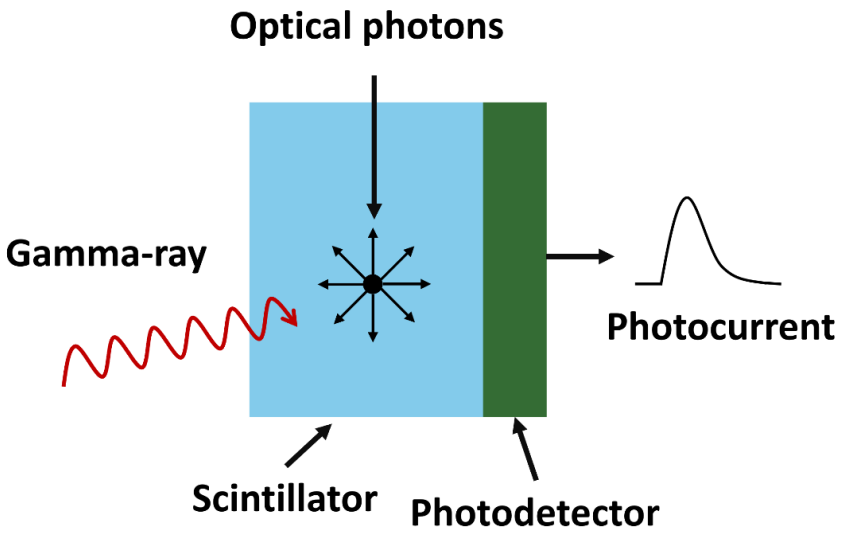

Figure 6. Illustration of the two main components of PET detectors, the scintillator, which absorbs gamma rays and produces lower energy photons, and the photodetector, which produces electric signals upon detecting the scintillation photons.

For a scintillator to be an effective absorbing medium, it must have a relatively high probability of interaction with the gamma rays, which is indicated by the attenuation coefficient of the scintillator. The attenuation coefficient of a scintillator affects the amount of material required to achieve a certain detection efficiency; scintillators with a lower attenuation coefficient can be made with less material and reduce the size of the detector. Additionally, it is preferable to have a scintillator with a high attenuation coefficient for photoelectric absorption compared to Compton scatter. Table 4 shows properties of common solid, inorganic, scintillators used for detecting photons with energy ~511 keV. This table shows that BGO, LYSO, and LSO are the three most dense scintillators with the highest attenuation coefficients, with BGO having a higher ratio between photoelectric absorption and Compton scatter. However, Compton scatter accounts for a significant fraction of interactions even in scintillators with a high effective atomic number, Z_{eff}.

Another important property of a scintillator is its light yield, which refers to the number of scintillation photons generated for a given amount of energy deposited in the material. Statistical fluctuations in the number of scintillation photons detected by the photosensors introduce noise in the output signals. These fluctuations are governed by Poisson counting statistics and are

proportional to $1/\sqrt{N}$, where N is the number of detected scintillation photons[2]. Therefore, scintillators with a high light yield are chosen to reduce the statistical fluctuations in the detected signals and improve the accuracy of position and energy measurements. Although BGO has a higher stopping power compared to LYSO and LSO, Table 4 shows that LYSO and LSO have a significantly higher light output. Furthermore, while NaI has the highest light output, it has a very low attenuation coefficient and a low ratio between photoelectric absorption and Compton interaction.

Table 4. Physical properties of common scintillators for PET. Source: table adapted from Lecomte et al.[8]

Scintillator	Density (g/cm^3)	Light output R (10^3 photons /MeV)	Decay time (ns)	Index of refraction	Attenuation coefficient at 511 keV (1/cm)	Ratio between photoelectric and Compton
Sodium iodide [NaI(TI)]	3.67	41	230	1.85	0.39	0.22
Bismuth Germanate (BGO)	7.13	9	300	2.15	0.89	0.78
Lutetium-Yttrium Oxyorthosilicate (LYSO:Ce)	7.19	30	40	1.81	0.79	0.49
Lutetium Oxyorthosilicate (LSO:Ce)	7.35	30	40	1.82	0.81	0.52
Gadolinium Oxyorthosilicate (GSO:Ce)	6.71	8	60	1.85	0.67	0.35
Yttrium Aluminium Perovskite (YAP:Ce)	5.5	17	30	1.95	0.47	0.05

The third key characteristic of a scintillator is the decay time, which is the time over which the scintillation light is produced. Using a fast scintillator with a short decay time reduces the time needed to collect the scintillation light. This means that the detector can quickly become available to detect the next signal, reducing the processing time needed between subsequent signals, also called deadtime. Table 4 shows that LYSO and LSO have a short decay time of 47 ns. Together, a high stopping power and light output and a short decay time make LSO a promising candidate for applications in PET imaging.

1.3.2. Solid State Photosensors

New generation and emerging PET detectors mainly use solid state photosensors, called silicon photomultipliers (SiPM), for detecting scintillation light. The building block of the SiPM is a photodiode called the single photon avalanche diode (SPAD) and it is operated in reverse bias above the breakdown voltage where self-sustained avalanche processes can occur, Figure 7[9].

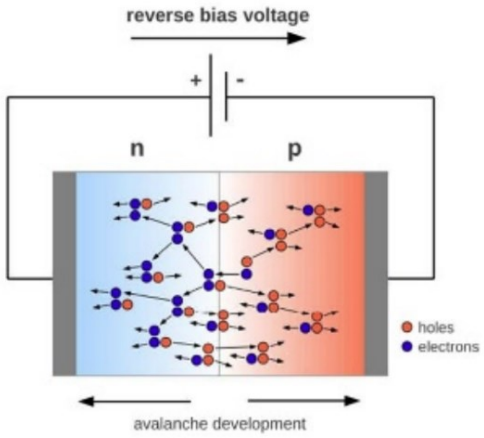

Figure 7. Avalanche process in a SPAD which is operated above the breakdown voltage. Source: image adapted from Gundacker et al.[10]

The avalanche is initiated when a photon from the scintillation light is absorbed in the depletion region of the photodiode and generates an electron-hole (e-h) pair. The electric field accelerates the e-h pair towards opposite terminals of the pn junction with the electrons and holes being accelerated towards the n-doped and p-doped connections, respectively. Since the SPAD is above the breakdown voltage, both the electrons and holes gain sufficient kinetic energy to create secondary e-h pairs during collisions through impact ionization. The secondary e-h pairs

also undergo impact ionization, with each e-h pair undergoing impact ionization several times, and this process causes a rapid gain of e-h pairs which results in a diverging electrical current. The avalanche is quenched using a series quenching resistor connected to the SPAD. The photocurrent produces a voltage drop across the quenching resistor which, in turn, lowers the voltage across the photodiode below the breakdown voltage and quenches the avalanche. The gain associated with the SPAD is defined as the number of charge carriers collected per avalanche. The gain is dependent on the voltage, since increasing the voltage above breakdown further increases the strength of the electric field and thus the amplification of the e-h pairs.

A single SPAD produces the same signal regardless of the number of photons striking it and cannot differentiate between one or several photons detected. To count the number of photons, many thousands of SPADs are connected in parallel to form a SiPM[10], which is a few millimeters wide, Figure 8. The signals from each SPAD are summed and the output signal is proportional to the number of fired SPADs in the SiPM. The output signal from the SiPM is also proportional to the number of photons since the scintillation photons are spread out to trigger different SPADs in the SiPM. The SiPMs are arranged into an array, and the total energy deposited in the scintillator can be calculated by summing signals from each individual SiPM in the array. This summed signal is proportional to the total number of scintillation photons. Therefore, the amplitude of a signal produced is proportional to the intensity of the light signal incident on the SiPM and thus also to the energy deposited in the scintillator by the gamma rays. However, saturation effects are observed if the impinging light flux is higher than the available SPAD density. SiPMs are manufactured with a higher density of SPADs to avoid saturation effects to help maintain the dynamic range.

The high gain provided by SiPMs, ranging from 10^5 to 10^7,[11] is desirable in PET detectors because the scintillation light is relatively weak, and a high amplification of photocurrent is needed to ensure a high signal-to-noise ratio and energy resolution. A high gain also permits the use of off-the shelf preamplifiers in the signal readout. Another key parameter of SiPMs is the photon detection efficiency (PDE), which is defined as the probability of an incident photon delivering a measurable signal. The PDE depends on the probability of a photon being absorbed in silicon and generating an electron-hole pair (quantum efficiency), the likelihood of an electron or hole initiating an avalanche (avalanche triggering probability), and the geometric fill factor.

The PDE has a strong dependence on the photon wavelength and the overvoltage. State-of-the-art SiPMs can reach PDE up to 60% at 410 nm which makes them ideal candidates for detecting light from LYSO scintillators since this wavelength matches the peak emission from LYSO[9].

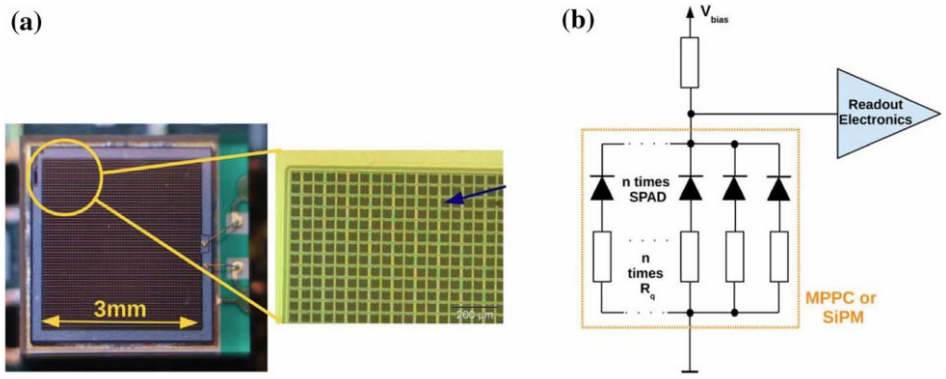

Figure 8. A) Analog SiPM with a zoom on the individual SPADs. B) Electrical diagram with all SPADs and series quenching resistors all connected in parallel to form a SiPM. Source: image adopted from Gundacker et al.[10]

A major source of noise from SiPM photodetectors is dark current. Thermally generated electron-hole pairs can initiate an avalanche and result in a current, called dark current, which is indistinguishable from current generated by a photon. Dark current increases with the overvoltage (which increases the avalanche triggering probability) and the temperature (which increases the probability of thermally generated e-h pairs). The photosensors can be cooled to reduce the operating temperature of the SiPM and limit the contribution of dark current to the signal-to-noise ratio.

1.3.3. Block Detector

Conventional whole-body PET (WB-PET) systems utilize ring detector design to surround a patient body. Rings are formed by assembling individual detector units, or block detectors, consisting of a scintillator optically coupled to a photosensor. Figure 9 shows the evolution of block detector designs from the early developmental years of PET to the recent 2010s[15]. Early designs involved a one-to-one coupling of a scintillator with a photomultiplier tube (PMT) as the photosensor. Subsequent designs featured large blocks of scintillators segmented into an array of smaller pixels to achieve a better spatial resolution. However, due to the high cost of PMTs and

bulkiness, the one-to-one coupling became impractical with an increase in the number of scintillation pixels. So, the pixelated scintillator was coupled to four PMTs in a light-sharing design, enabling the reduction in scintillator pixel size. In the light sharing design, each pixel is optically isolated from other pixels using reflective materials that filled the cuts. The depth of the cuts is designed such that the light distribution over the four photosensors depends on the pixel which interacted with the annihilation photon. Upon detecting the scintillation light, each of the four photosensors produce a signal which can be used to calculate the pixel which interacted with the gamma photon. The coordinate calculation is performed using the so-called Anger Logic and which is expressed as:

$X = \left(\frac{A + B - C - D}{A + B + C + D}\right)$	*14*
$Y = \left(\frac{A + D - B - C}{A + B + C + D}\right)$	

Where A, B, C, and D are the signals from each of the four PMTs. The number of scintillator elements continued to increase in the following years and LYSO/LSO became the scintillator of choice in most PET detectors due to its fast and bright scintillation properties compared to BGO and NaI. By 2010s advancements in solid-state photosensors enabled the adoption of avalanche photodiodes and silicon photomultipliers in newer PET detectors, replacing PMTs. The pixelated scintillators and solid-state photosensor are used in a similar light sharing scheme with Anger logic being used for coordinate calculation. However, SiPMs provide comparable timing resolution and gain as PMTs while offering notable advantages over PMTs such as improved photon detection efficiency, lower power consumption, magnetic field compatibility, and compactness, which enables a higher ratio of scintillation pixel to photosensor for a more precise determination of the location of interaction[12],[13],[14].

The design of the block detectors and their arrangement into a complete PET detector determines the spatial resolution and system sensitivity. Both of these quantities impact clinical parameters such as the image quality, lesion detectability, injected radioactivity and patient dose, and scan duration, which are discussed later.

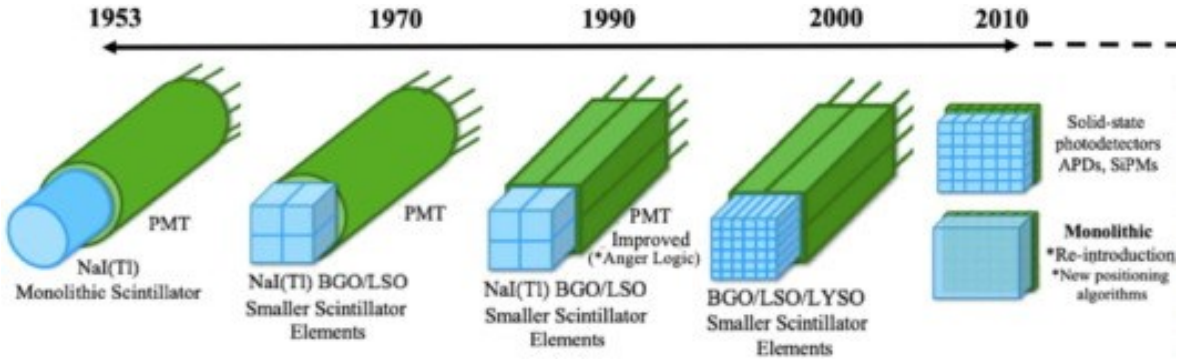

Figure 9. Evolution of the architecture of PET block detectors. Image adopted from Zatcepin et al.[15]

1.3.4. Coincidence Mode and Types of Coincidences

To provide measurements of two coincident gamma-photons along a given LOR, the individual PET block detectors work in coincidence mode. Signals are registered only when a pair of detectors is triggered within a specified interval of time, called the coincidence timing window, which may range from a few hundred picoseconds to a few nanoseconds. A true coincidence event occurs when a pair of detectors registers unattenuated gamma rays originating from the same annihilation event. This is an ideal scenario, and, in practice, PET data consists of different types of coincidences, shown in Figure 10, which degrade the position and energy measurements. The photons may undergo Compton scattering within the patient's body, losing energy and changing direction in the process. These events are termed scatter coincidences and the LORs generated using these coincidences may deviate significantly from the location of annihilation. Random coincidence refers to the simultaneous detection of two gamma rays originating from separate annihilation events. Some scintillators may contain intrinsic radioactivity and emit gamma rays, which may also be detected as random coincidences. The LORs associated with these events do not contain any information about the location of annihilation and add background noise in the images. Finally, at high count rates, three or more detectors may be involved in the detection of annihilation photons originating from separate annihilation events within the same coincidence timing window. For example, we may detect a pair of true coincidences and a single photon from a separate annihilation event. In this case,

there are three possible LORs, only one of which is true, and the data is normally discarded because of this ambiguity.

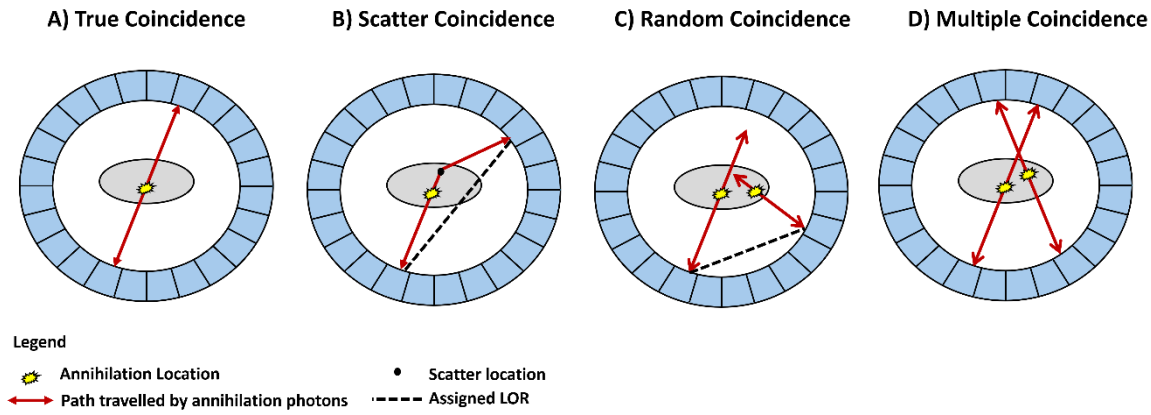

Figure 10. Illustration of different types of interactions of gamma rays that can be registered as coincidence events by PET detectors. A) True coincidence occurs when both annihilation photons escape the body unattenuated and are detected by a pair of detectors. B) Scattered coincidence occurs when one or both annihilation photons are scattered and change their trajectory before being detected by a pair of detectors. C) Random coincidence is generated when photons from two different annihilation events are detected by a pair of detectors. D) Multiple coincidence occurs when three or more photons from separation annihilation events are registered within the same coincidence timing window.

1.4. Performance Metrics for PET Detectors

1.4.1. System Count Sensitivity

One of the most important characteristics of a PET detector is the system count sensitivity, which is the number of events detected, in counts per second, per unit of radioactive concentration, in cps/Bq/ml for a given phantom. An improvement in system count sensitivity indicates improved count rates, which leads to better SNR and overall image quality. The system count sensitivity depends on two key factors: coincidence detection efficiency and the geometric efficiency of the detectors.

The detection efficiency of a single detector $n_{detector}$ depends on the stopping power of the scintillator, which in turn depends on the attenuation coefficient μ and the thickness of the

scintillator d, and the size of the energy window Φ. The coincidence detection efficiency for detecting a pair of annihilation photons is then given by the square of the single detection efficiency[2]:

$\eta^2_{detector} = (1 - e^{-\mu d})^2 \times \Phi^2$	*15*

The geometric efficiency $\eta_{geometric}$ is given by the product of the solid angle coverage of the detectors and the packing fraction, $\Omega \times \phi$. For ring detectors, the solid angle coverage depends on the detector diameter D and axial length of the detectors:

$\Omega = 4\pi \sin\left[arctan\frac{A}{D}\right]$	*16*

The detector diameter and axial length should be selected to optimize the solid angle coverage for the imaging task at hand. The packing fraction is given by the ratio of the active detection area to the total area of the detectors including dead space arising from gaps needed for reflective material between scintillation pixels:

$\phi = \frac{active\ area}{active\ area + dead\ space}$	*17*

The overall system count sensitivity for a point source at the center of a ring detector is given in Eq. 18.

$\eta = \eta^2_{detector}\eta_{geometric}$	*18*

The system count sensitivity also depends on the location of the phantom inside the FOV. For a point source of radioactivity, the sensitivity will be highest when the source is placed at the center and lowest when it is placed at the edges of the detector.

1.4.2. Spatial Resolution

The fundamental limit of spatial resolution in PET detectors is governed by the positron range and the non-collinearity between the annihilation photons which has been discussed previously. The positron range depends on the initial energy of the positron and the effective atomic number of the surrounding material. The noncollinearity is independent of the radionuclide because the positron must lose almost all its kinetic energy before annihilating. However, the blurring effect due to noncollinearity grows linearly with the diameter of the PET detector, as shown in Eq. 7. The remaining practical factors which contribute to the spatial resolution arise from the geometry and physical properties of the PET detectors.

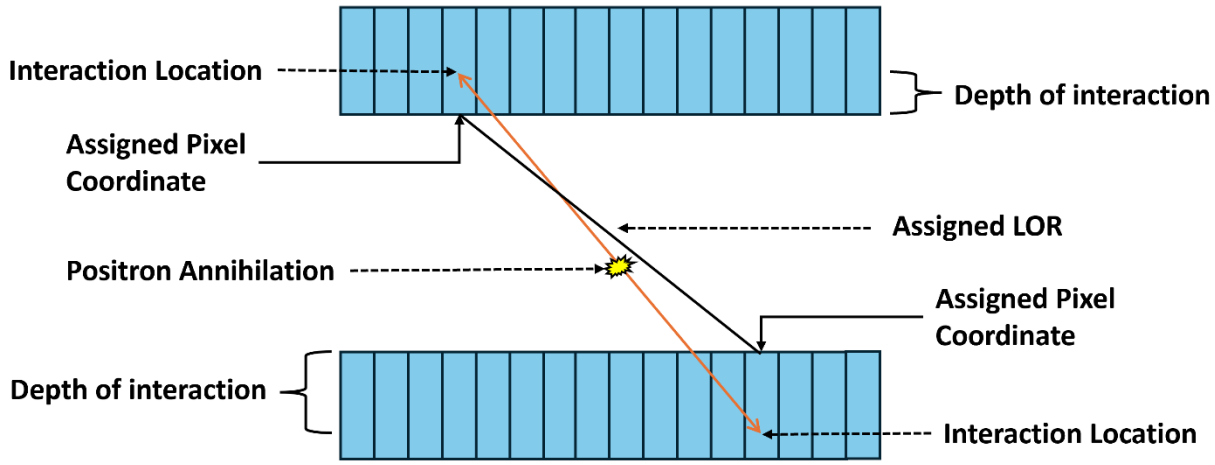

Figure 11. Illustration of the parallax effect. The annihilation photons interact at a certain depth within the scintillator and this depth is not measured by the detectors. The coordinate of interact is instead assigned to the surface of the scintillator and this leads to an inaccurate LOR which deviates from the location of annihilation.

For detectors using segmented scintillators, the resolution is limited by the size of the scintillator pixels, because the position of interaction within the crystal is not determined. Therefore, using smaller scintillator pixels leads to a better sampling and a higher spatial resolution. The spatial resolution is also affected by the so-called parallax effect, which occurs when the depth of interaction (DOI) of the gamma rays in the scintillator is unknown and the lack of DOI information causes mispositioning of the LOR (Figure 11). Gamma rays entering the scintillator at oblique angles may interact and deposit energy in a neighboring pixel. Without DOI

information, the coordinate of interaction is assigned to the surface of the detector element that absorbed the radiation, which is the neighboring pixel in this example. An incorrect assignment of the interaction coordinate causes a deviation of the assumed LOR from the true LOR and degrades the spatial resolution. The parallax effect worsens with oblique incident angles of annihilation photons, as shown in Figure 11. The parallax effect also depends on the scintillator depth since a longer scintillator, despite providing a higher stopping power and detection efficiency, increases the likelihood of interaction in a neighboring crystal. For this reason, the scintillator depth is selected to optimize the system sensitivity while minimizing the parallax effect. The spatial resolution of a PET detector is also influenced by the angular coverage of the detectors, as discussed further below.

1.4.3. Recovery Coefficient

The limited spatial resolution of a PET detector manifests as the partial volume effect (PVE) in reconstructed images. The PVE is evident with a point source of activity, which appears as a blob in the images with a characteristic size equal to the point spread function (PSF) of the detector. The PVE causes an apparent spill-out of counts from an object, leading to underestimation of activity concentration inside the object in reconstructed PET images. PVE can be characterized using the recovery coefficient, which is a ratio between the activity concentration measured in the image to the true activity concentration of the object. The RC can be measured by filling different sized spheres with the same activity concentration and then calculating the ratio given in Eq. 19.

$$RC = \frac{Measured\ peak\ activity\ concentration}{True\ activity\ concentration} \quad (19)$$

Figure 12 illustrates show the PVE affects the activity concentration of spheres with different diameters, and it also shows the RCs for each sphere measured with a WB-PET scanner. The activity concentration is accurately recovered for larger spheres with diameter three times the 10 mm spatial resolution because these spheres are not significantly affected by the PVE. However, the activity concentration begins to drop significantly as the sphere diameter decreases and approaches the 10 mm spatial resolution. This is indicated by a suppression in the peak activity

concentration and a diminishing plateau of the measured activity concentration across the sphere. As shown, less than half of the true activity concentration is recovered in the 10 mm sphere.

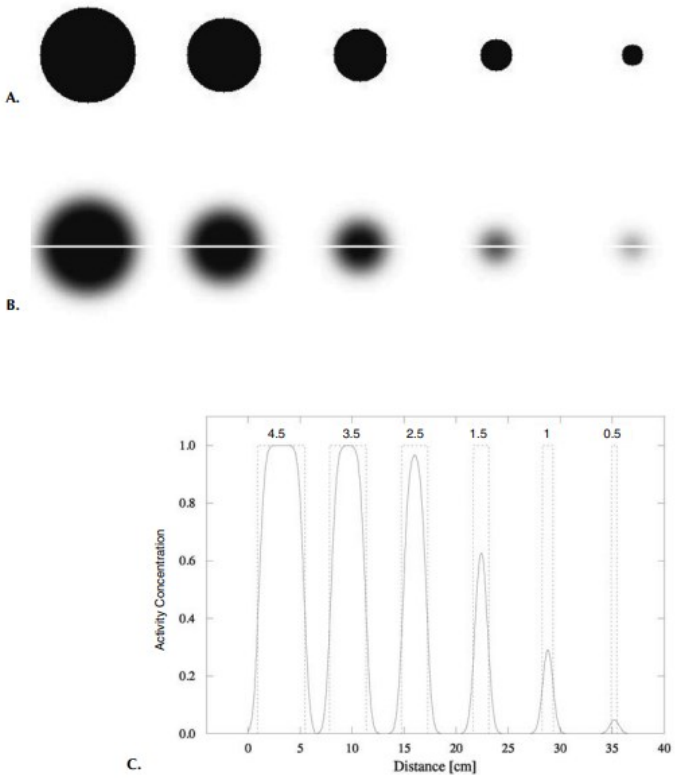

Figure 12. A) Six sphere phantoms with diameter 4.5, 3.5, 2.5, 1.5, 1, 0.5 mm containing the true activity concentration. B) Reconstructed images of the six sphere phantoms. C) Normalized activity concentrations each sphere calculated using Eq. 19. Source: image adopted from Cherry et al., 2006[2]

The RC provides a good indication of lesion detectability using a given PET detector and determines its quantitative accuracy. The RC is affected by the spatial resolution, system sensitivity, and energy resolution of a PET detector. An improvement in the spatial resolution of a detector reduces the PVE, resulting in a lower spill-out of counts between different objects and an improvement in the RC of small objects. However, this is possible if the system count sensitivity is high enough to support the improved resolution; a detector with a high spatial resolution but an insufficient sensitivity will result in a poor signal-to-noise ratio, and this hinders improvements in the RC[16,20]. Finally, the RC may also be degraded by scattered events

and a sufficient energy resolution is needed to allow for appropriate discrimination of the scattered coincidences.

1.5. Comparison of PET Detector Designs

1.5.1. Whole-Body, Total-Body, and Organ-Targeted PET

Whole-body (WB) PET detectors have continued to be the most commonly used detector design in PET imaging. WB-PET detectors consist of a ring (or several rings) of detectors which surrounds the patient, and the detectors only partially cover the detector, Figure 13. The patient lies on a bed which moves them through the detector while performing acquisition in a step-and-shoot fashion. Most clinical WB-PET scanners consist of block detectors with scintillators segmented into crystals of size $4\text{mm} \times 4\text{mm} \times 20mm$ made of LYSO or LSO[17,18,19]. The scintillators are coupled to solid state photosensors, such as SiPMs, in newer generation detectors meanwhile older PET detectors still use PMTs. In these scanners, the axial field-of-view (aFOV) is defined as the length of the detector and transverse field-of-view (tFOV) is defined as the diameter of the detector. The aFOV in WB-PET detectors ranges between 160 mm to 250 mm and the tFOV ranges between 580 mm to 764 mm to fit the patients inside scanner bore.

Virtually all clinical WB-PET scanners are now integrated with Computed Tomography (CT) scanners in combined dual-modality PET/CT systems. These systems allow for the accurate correlation of anatomical structure (CT) with physiological function (PET), providing more comprehensive diagnostic capabilities. In oncology, where the most common radiotracer used is 18F-fluoro-2-deoxyglucose (18F-FDG), the PET component highlights areas of increased metabolic activity, while CT component provides detailed anatomical images, identifying the precise location and size of areas with higher 18F-FDG uptake, such as tumors within the body. PET/CT's most widespread application has been for the detection of metastasis, staging of cancer, differentiation between malignant and benign lesions, treatment planning, evaluation of treatment efficacy and detection of recurrent disease. However, these scanners still have suboptimal detector characteristics. For example, even the highest performing WB-PET detector such as has 1% sensitivity, which means that they detect only 1% of the incoming radiation[20]. In terms of count rate per unit of radioactivity, the total sensitivity ranges between 5-20 cps/kBq[21]. The spatial resolution for these scanners ranges between 4-6 mm FWHM. The recovery coefficients for large spheres, 37 mm in diameter, ranges between 0.7-0.9 while for smaller

spheres, 10 mm in diameter, ranges between 0.20-0.50. The poor sensitivity necessitates comparatively high doses of 18F-FDG to be administered, typically amounting to around 7.5 mSv[22]. This level of radiation exposure raises significant safety concerns, limiting the widespread clinical application of this otherwise powerful imaging modality. Consequently, PET imaging is primarily used for already diagnosed patients to plan and monitor treatment response and disease progression, rather than for general screening purposes or in pediatric populations where radiation exposure is a particularly critical concern.

WB-PET imaging is generally associated with the highest radiation exposure among medical imaging modalities, with injected radioactivity ranging from 200-500 MBq[23,24,25]. The total number of events detected by the PET scanner depends on the system sensitivity and the radioactivity in the FOV. Therefore, significant reduction in the injected radioactivity to lower the radiation exposure requires significant improvements in the system sensitivity. A higher sensitivity PET detector can be achieved by 1) using thicker crystals, to increase the stopping power and the detection efficiency, or 2) by increasing the solid angle coverage by either extending the aFOV or reducing the ring diameter. Approaches that involve the use of thicker crystals or extending the aFOV increase the total volume of scintillators. This prompts the question: which approach (thicker crystals or larger aFOV) provides a higher sensitivity for a fixed total volume of scintillators? Simulations performed to study the trade-offs between these approaches demonstrated that increasing the aFOV enables a higher system sensitivity instead of crystal thickness for a fixed crystal volume[26,27]. Besides, increasing the crystal thickness would lead to a higher parallax error which degrades the spatial resolution of the detector. Meanwhile, there is a greater room for improvement in the geometric efficiency because in a typical WB-PET detectors, the probability of a gamma photon interacting in a 20 mm long LSO scintillator is 82% but the probability of a gamma photon arriving at the ring is only 35%.

An example of a clinical PET scanner with a long aFOV is the Biograph Vision Quadra with an aFOV of 106 cm and tFOV of 78 cm[28]. This detector is essentially created by axially concatenating 4 subsystems of an existing WB-PET scanner. The long aFOV scanner has a larger solid angle coverage which increases the total sensitivity to 175.3 cps/kBq compared to 5-20 cps/kBq for standard WB-PET. Improved sensitivity permits the use of finer crystal pixels, $3.2 \times 3.2 \times 20$ mm in size, to increase the spatial resolution, which is ~3.5 mm at the center

FOV and ~4.4 mm at a radial offset due to parallax error. The Biograph Vision Quadra demonstrates improved lesion detectability with an improved RC of 0.78 for 10 mm spheres and 0.93 for 37 mm spheres. More recently, even longer aFOV detectors, called total-body (TB), PET detectors are being developed to encompass and collect signal from the entire adult human body, Figure 13. The world's first total-body PET detector is called the uExplorer and has an aFOV of 194 cm and and a tFOV of 78.6 cm[29]. There are 8 units in the axial direction with a 0.26 cm gap between the units. The scintillators are pixelated into crystals, each $2.76 \times 2.76 \times 18.1\ mm$ that are readout using four $6 \times 6\ mm$ SiPMs in a light sharing scheme. The system sensitivity was measured to be 174 cps/kBq (17%) at the center FOV and the spatial resolution was measured to be ~3.0 mm at the center FOV and ~4.0 mm at a radial offset of 20 cm from the center. The RC was measured with a sphere-to-background concentration ratio of 3.7 to be 1.0 for 37 mm sphere and 0.6 for 10 mm sphere.

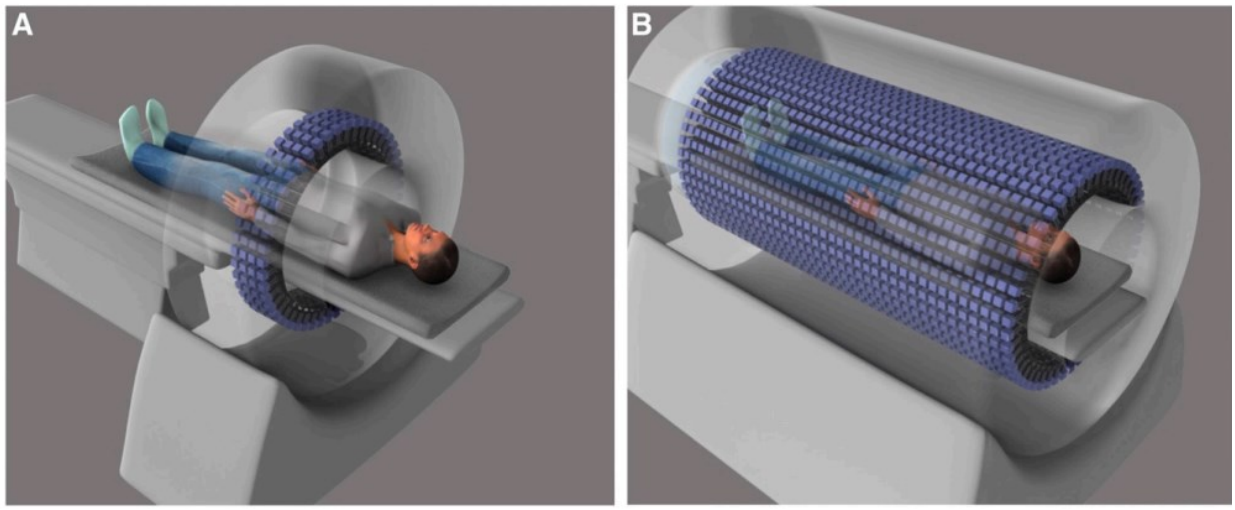

Figure 13. Schematic of a WB-PET system (left), a TB-PET system (right), and the sensitivity and acquisition times corresponding to the two systems. Source: image adopted from Cherry et al., 2018.[30]

The higher number of count rate, enabled by improved system sensitivity, can be used to optimize the different count-dependent clinical parameters depending on the task at hand. The first option is to keep the acquisition time and administered dose equal to current standards and use the higher sensitivity to improve the SNR. The second option is to keep the administered dose and SNR equal to current standard and reduce the acquisition time to improve the patient

throughput or to perform dynamic imaging. The final option is to reduce the administered dose while maintaining the acquisition time and SNR. However, it is not possible to simultaneously optimize all clinical parameters since all three parameters affect the number of acquired counts. For example, it is not possible to reduce both administered dose and acquisition time because it will result in a low SNR.

Table 5. Fraction of solid angle coverage for WB-PET, TB-PET, and organ-targeted PET ring detectors calculated using Eq. 16.

Detector Design	Standard WB-PET	TB-PET		Organ-targeted PET	
aFOV (cm)	25	100	190	25	25
tFOV (cm)	70	70	70	15	10
Fraction of solid angle coverage	0.34	0.82	0.94	0.86	0.93

The main disadvantage of increasing the detector components to build a TB-PET system is the cost associated with the higher number of scintillators and photosensors; increasing a PET/CT detector from 20 cm aFOV to 100 cm aFOV increases the cost by a factor of 4 and increasing from 20 cm aFOV to 200 cm aFOV increase the cost by a factor of 7.7[20]. As an alternative approach, the solid angle coverage of the detectors can be increased by reducing the detector diameter. This approach reduces the required amount of detector components and thus the costs. Table 5 demonstrates that a similar solid angle coverage can be achieved by reducing the detector diameter as with extending the aFOV for a TB-PET.

Reducing the detector diameter restricts the total region of the body that can be imaged at any given time which means that the detector will be best suited for imaging tasks which require scanning individual organs. Indeed, applications for PET imaging increasingly involve the visualization of specific organs with dedicated systems, such as in breast or prostate cancer detection and treatment monitoring, neuroimaging, or cardiac imaging (Figure 14). Organ-targeted detectors are typically optimized to scan a single organ of interest which also reduces the signal from other parts of the body and maximizes the number of annihilation photons collected from the single organ[21,31]. Furthermore, the noncollinearity effect becomes less significant in smaller diameter PET detectors and the scintillator crystal pixel size starts to

dominate the overall spatial resolution. So, organ-targeted detectors are designed with a relatively small crystal pixel size, ~2.5 mm in width. However, the parallax effect becomes more significant in detectors with smaller diameters, and this necessitates reducing the thickness of scintillators or implementing logic to collect DOI information.

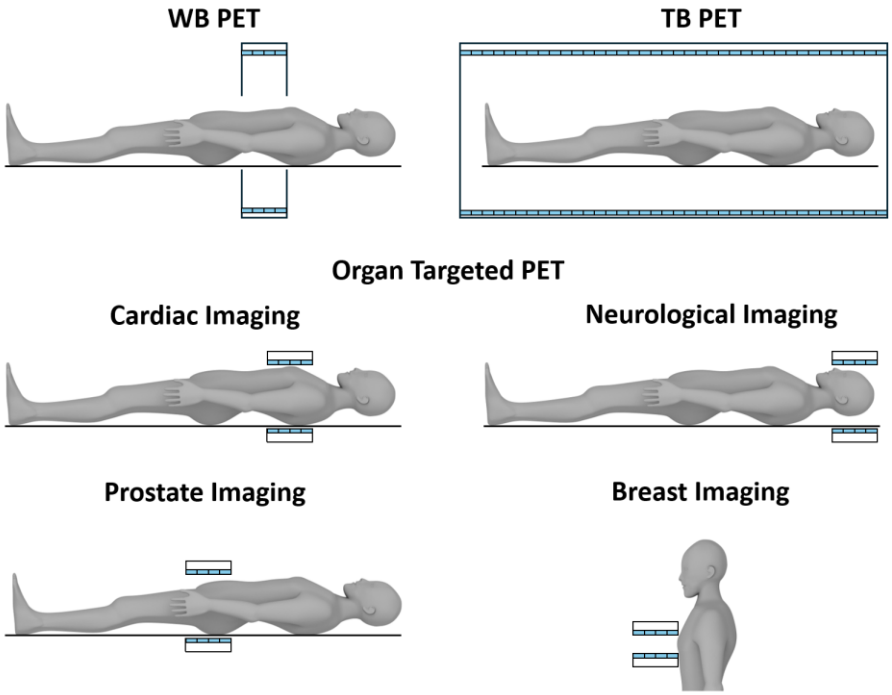

Figure 14. Detector orientations and patient positioning between detectors for different clinical applications of Radialis PET.

1.5.2. Planar Geometry for Organ-Targeted PET

The common approach with designing organ targeted PET detector has been to optimize the detector size for a single organ of interest. However, an adjustable detector size may be advantageous for scanning multiple organs (breast, brain, prostate) as schematically shown in Figure 14 above. An adjustable detector design can be achieved using a set of two planar detectors, each set comprising of several block detectors, which are placed on opposing sides of an organ and work in coincidence mode. The separation between the two planar detectors can be adjusted and the detectors can be rotated. Planar detectors can achieve a higher solid angle coverage compared to WB-PET by optimizing both the surface area of the detectors (detector width and aFOV) and detector distance to the organ (separation). For imaging multiple organs,

the detectors need to be designed to ensure sufficient solid angle coverage, and thus geometric efficiency, for a range of working separations.

The spatial resolution of ring and planar PET systems is directly affected by the detector geometries due to the variation in the parallax effect and the angular coverage. The parallax effect manifests differently in the two detectors. Recall that annihilation photons entering the detector surface at oblique angles may penetrate the first detector they strike and be detected by an adjacent detector, thus contributing more significantly to the parallax effect compared to photons entering perpendicular to the detectors. In ring geometry, the fraction of annihilation photons entering at oblique angles to the detector surface increases as the source of radiation is moved radially towards the edge of the ring. This means that the parallax effect is nonuniform in ring detectors, becoming more significant as the source is offset radially. Consequently, the resolution in the radial direction deteriorates as the source moves towards the periphery of the FOV. As for the planar PET detector geometry, the parallax effect (Figure 11) at the center of planar detectors is more pronounced compared to ring detectors. This is because a larger fraction of annihilation photons emerging from the center of a planar detector enter the detector at oblique angles. However, the parallax effect remains uniform in planar detectors as the source of radiation is moved towards the periphery of the FOV. Furthermore, planar PET detectors have a lower angular coverage compared to ring detectors. The limited angular coverage introduces challenges in accurate image reconstruction which ultimately degrades the axial spatial resolution in planar PET detectors.

1.6. Image Reconstruction in Limited Angle Planar PET Detectors

The goal of image reconstruction is to use the data acquired from the detection of annihilation photons to determine the distribution of the radiotracers inside the patient body. The image reconstruction methods can be grouped into two categories 1) analytical and 2) iterative algorithms. Analytical algorithms are less computationally intensive compared to iterative algorithms; however, analytical algorithms make idealized assumptions about the detection process and the collected data. Iterative algorithms incorporate a realistic model of the PET detectors which can lead to improved spatial resolution[32,33,34,35]. Additionally, accurate reconstruction demands adequate linear and angular sampling. Iterative algorithms are less prone to artifacts from missing data compared to analytical algorithms[2]. Due to these advantages and

technological advances in computational acceleration methods, iterative algorithms are being adopted in modern and new generation of PET detectors.

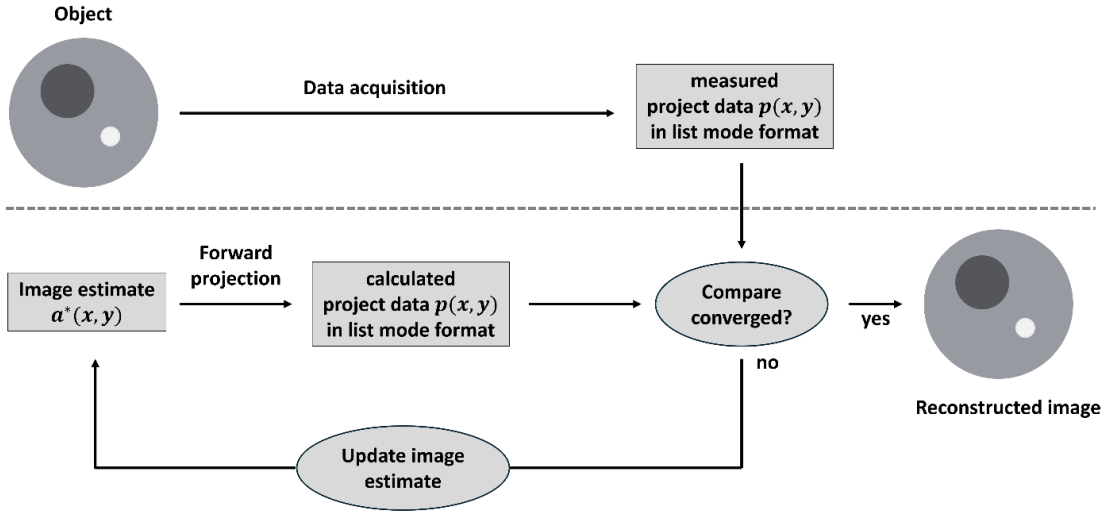

Figure 15. Flowchart of an iterative image reconstruction algorithm. Source: image adapted from Cherry et al., 2006.[2]

The first step in image reconstruction is initializing the image space by defining the number and size of voxels, which are essentially three-dimensional pixels. The general approach to iterative reconstruction is shown in Figure 15. The reconstruction begins with an initial guess for the image containing the radioactivity distribution. This can be a blank or uniform grayscale image. Then, an operation called forward projection is performed to calculate an estimated projection dataset based on the initial image. There are a finite set of LORs that can be acquired by a PET detector and these LORs are defined by pairs of opposing detector elements. Projection data refers to the collection of LORs and weights associated with each LOR. Forward projection calculates the weights associated with each LOR by summing all the activity in pixels that are intersected by each LOR. Next, the estimated projection dataset is compared with the measured projection dataset acquired by the PET detector. A cost function is used to calculate the difference between the estimated and measured projections, and it is the cost function that is optimized during reconstruction. Finally, the result from the cost function is used in an update function to update the image estimate in a process called backprojection. This process is

performed iteratively until the cost function is optimized and eventually, the estimated image converges to the radioactivity distribution.

There are different iterative algorithms and are classified by the cost function, update function, how the detection process is modelled, how data statistics are modelled and how prior information is implemented. A model of the detection process can be integrated during the forward projection which models the probability that annihilation photons emitted from a point in the image will be detected in a given detector element. The models can include details about the system geometry, object scatter, detector characteristics, positron range, and noncollinearity.

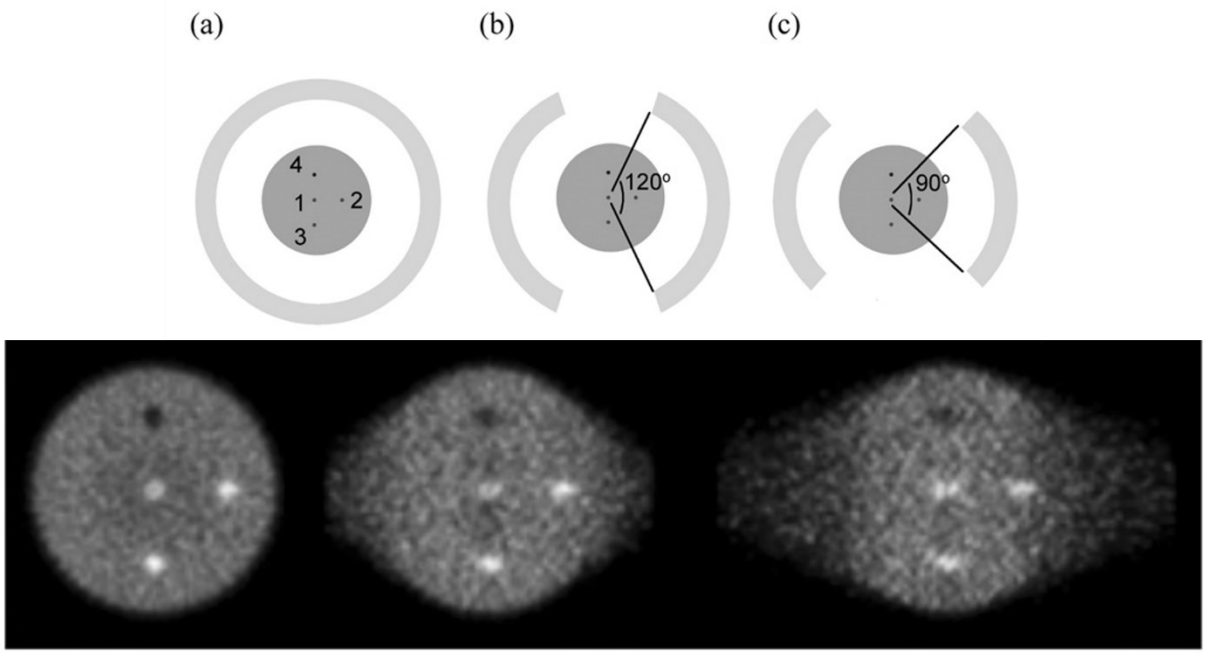

Figure 16. Simulation study using ring and partial ring detectors with different angular coverage and a phantom imaged in the center of these detectors (top). Reconstructed images from detectors with full (ring) and limited (partial ring) angular coverage, demonstrating smearing in the images reconstructed with detectors that have limited angular coverage, similar to planar PET detectors (bottom)[36].

The image quality of the reconstructed image is limited by the statistical quality of the data, the detector resolution, and, importantly, the angular coverage and sampling. Angular coverage is defined by the maximum angle subtended by the detectors around the object and angular

sampling is defined by the size of the detector elements. Limited angular coverage leads to image artifacts, particularly smearing of objects, which ultimately affect the apparent lesion size and contrast. Fundamentally, the requirement for complete angular coverage around the object arises from the uncertainty in the location of annihilation along a given LOR. To minimize smearing, a set of LORs covering 180° around the object is required, which can be achieved using ring detectors as shown in the simulation study in Figure 16. However, the same simulation shows that with partial ring detectors, which mimic the limited angular coverage of planar PET detectors, significant smearing occurs because of incomplete sampling of LORs around the object.

The uncertainty in the annihilation location can be reduced using time of flight (TOF) measurements, which requires measuring the arrival time of photons. Photons that originate at the center FOV will arrive at the detectors simultaneously but photons originating at increasing distance from the center FOV will have larger difference in their arrival times. Therefore, TOF leverages differences in arrival times of the annihilation photons at the detectors to narrow the probability distribution of annihilations along the LOR. The possible increase in spatial resolution using TOF PET is determined by the timing resolution of the detectors. Eq. 20 relates the difference in arrival times of the two annihilation photons Δt originating from distance d from the center FOV. From this equation, we can estimate that a timing resolution of 100 ps is needed for a spatial resolution of at least 15 mm, while the timing resolution of current state-of-the-art detectors ranges between 200-500 ps[37,38]. However, there is still significant degradation of spatial resolution in limited-angle planar PET detectors with TOF reconstruction and a timing resolution of 100 ps[39].

$$d = \frac{\Delta \mathrm{t} \times \mathrm{c}}{2}$$	*20*

The goal of this project is to optimize the image quality of a high-sensitivity planar organ-targeted PET detector by increasing the angular coverage through detector rotations and a fully 3D image reconstruction. Overcoming the problem of limited angular coverage is essential to optimize the spatial resolution of the system and fully leverage the high sensitivity of the organ-targeted PET detector.

2. Radialis Planar Organ Targeted PET

2.1. Detector Architecture

The organ targeted planar PET detector presented in this work was initially designed for breast imaging at an improved system count sensitivity and spatial resolution compared to WB-PET detectors (Figure 17). The PET detector consists of two planar detectors heads. The separation between the two detector heads can be adjusted and the two detectors can be rotated around the FOV. The detector is based on four-side tileable modules which are arranged seamlessly, without gaps or dead zones, into a 4×3 detector array to produce an active sensing area measuring $230.64\ mm \times 172.98\ mm$ (Figure 18). This detector provides a higher solid angle coverage of the breast compared to WB-PET due to an optimized aFOV, separation between the detector heads, and more finely segmented detector elements. This detector also has a variable angular coverage which depends on the separation between the detectors. Although the current detector geometry has been optimized for breast imaging, both the detector separation and the sensing area can be resized for multi-organ imaging.

Each detector unit is based on a Lutetium Ytrrium Oxyorthosilicate (LYSO) scintillator and SiPM photosensors, as shown in Figure 19. The scintillator is segmented into a 24×24 array of crystals with dimensions $57.66 \times 57.66\ mm$ and a thickness of $13mm$. The crystal pixels measure $2.56 \times 2.56\ mm$ and each pixel is separated by specular reflectors with thickness of $0.08\ mm$. Light from the scintillator is spread across an 8×8 pixelated array of photosensors, with an overall size of $57.40 \times 57.40 \times 7.2\ mm$. A monolithic light guide is used to optically couple the scintillator with the photosensors and spread the scintillation light across the photosensors. Following coincidence detection of gamma rays, signals from the photosensors are digitized and stored on a computer. The coordinates of interactions are calculated from the stored data, using Anger Logic, which is essentially a weighted average of the photosensor positions with the signal acquired from the photosensors. For each coincidence event, the coordinates of interactions and the energies for the photons are saved in a list mode file (LMF) which is used in image reconstruction.

Figure 17. Top: Radialis PEM camera with two planar detector heads positioned horizontally on both sides of the immobilized breast for imaging in the craniocaudal (CC) view. The detector heads can be lifted, with the separation between them adjusted to allow rotation and acquisition of images in the mediolateral oblique (MLO) view. Bottom: 3 × 4 array of sensor modules inside a detector head.

LMF generation involves filtering events to discard a fraction of scattered events and oblique LORs to reduce image blur. Scattered events are filtered by discarding events with energy outside a defined energy window of 350 keV to 700 keV. From the other side, the energy window width directly impacts system sensitivity and has been selected to balance the amount of scatter discrimination while maintaining the system sensitivity. In addition to the energy filter, an angular filter is also applied during LMF generation to minimize oblique LORs which are responsible for the parallax effect because the detector cannot measure DOI. The angular filter works by removing LORs which form an angle greater than 1 radian with the detector surface. The angular filter has also been selected to minimize the parallax effect while maintaining system count sensitivity.

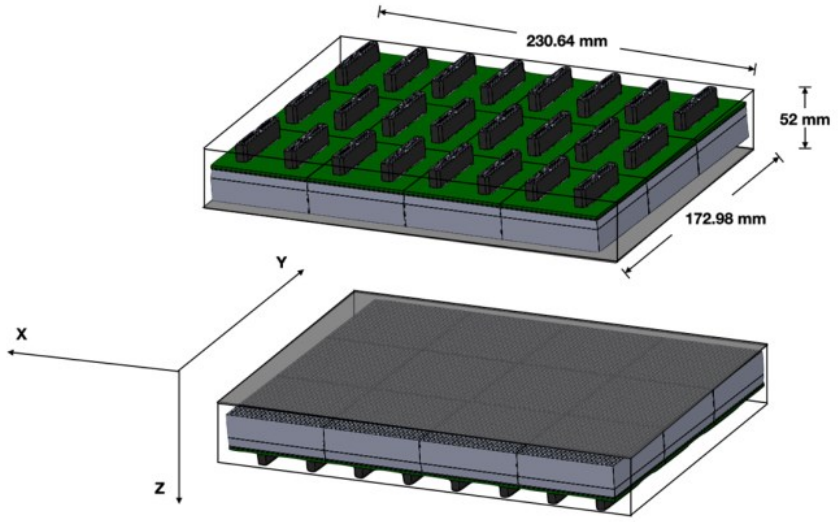

Figure 18. Schematic of two detector heads, each assembled with a 3 × 4 array of detector units, used in the Radialis PET camera. Source: image adopted from Baldassi et al.[40]

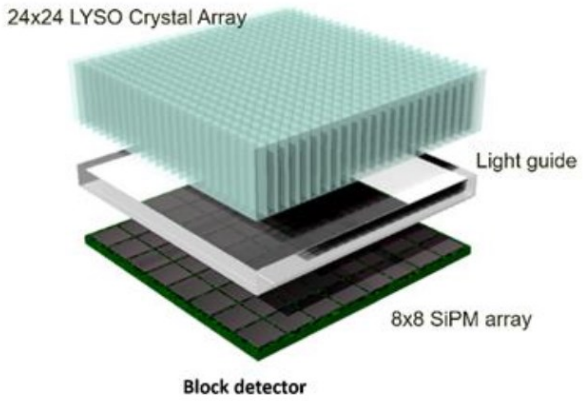

Figure 19. Design of a detector unit used in construction of the Radialis PET camera. Source: image adopted from Poladyan et al.[41]

2.2. MLEM Reconstruction

Image reconstruction in the Radialis PET detector is performed using an iterative reconstruction method called the Maximum Likelihood Expectation Maximization (MLEM), which is the most widely used form of iterative reconstruction. The MLEM is an iterative and statistical approach that assumes a Poisson distribution of the data. In MLEM, a statistical measure called the likelihood is maximized, using an algorithm called expectation maximization, when the

difference between the measured and estimated projections is minimized. The image reconstruction begins with an operation called forward projection, which calculates projection data based on the estimated image λ^k, at the current iteration k. The projection data contains counts received by all LORs and is calculated by determining the contribution of every voxel to a measured LOR:

$$s_{j_w} = \sum_i A_{j_w,i}\lambda_i \qquad 21$$

where s_{j_w} is the projection element containing the number of counts in LOR j_w, A is the System Matrix (SM) and it provides the probability that gamma rays from pixel i will be detected in LOR j_w. Here w indicates that only a subset of LORs which were measured by the detectors are considered for reconstruction. Next, the ratio between the measured projections, s'_{j_w}, and the calculated projections, s_{j_w} is calculated and this ratio indicates how well the estimated images describes the measured projection data. The ratio is then backprojected to the image space using the SM to determine the contribution of every measured LOR, s_{j_w}, to a voxel, i, and give a correction term, c_i:

$$c_i = \sum_{j_w} A_{j_w,i} \frac{s'_{j_w}}{s_{j_w}} \qquad 22$$

Finally, the correction term is multiplied by the voxel value in the estimated image, λ_i^k and then normalized by the sensitivity matrix $\sum_{j_w} A_{j_w,i}$ to generate a new estimate for the voxel λ_i^{k+1} for the next iteration:

$$\lambda_i^{k+1} = \frac{\lambda_i^k}{\sum_{j_w} A_{j_w,i}} \times c_i \qquad 23$$

These steps are performed until the algorithm converges or until a stop condition is met. A disadvantage of MLEM is that the image becomes noisy as the algorithm converges due to the bad conditioning of the problem. Therefore, the algorithm is stopped before convergence after 15

iterations. Additionally, a smoothing filter is applied after each iteration to reduce the image noise.

The image reconstruction produces a 3D image which is displayed as a set of 2D images (called slices) along a given axis. The image can be sliced along the x, y, or z axes of the detector and these axes are shown in Figure 18. Slices from the transverse and axial planes from a reconstructed image of a Na-22 point source with the Radialis planar PET detector are shown in Figure 20. The transverse plane is parallel to the detector heads and the axial plane is perpendicular to the detector heads. As shown in Figure 20, the spatial resolution along the z axis of the detector is significantly worse compared to the resolution along the x and y axis. The smearing of the point source in the direction perpendicular to the detectors, resulting in degraded spatial resolution, is a consequence of the limited angular coverage of the detector. In the center of the FOV, the angular coverage of the detectors in the XZ and YZ planes is 151° and 142°, respectively, when the detectors are separated by 60 mm; this corresponds to 84% and 78% of the complete 180° angular coverage required for image reconstruction. However, the angular coverage drops to 75° and 60° in the XZ and YZ planes, respectively, when the detector separation increases to 300 mm. Smearing due to the limited angular coverage of the detectors results in inaccurate distribution of radioactivity in the FOV and degrades the recovery coefficient of objects.

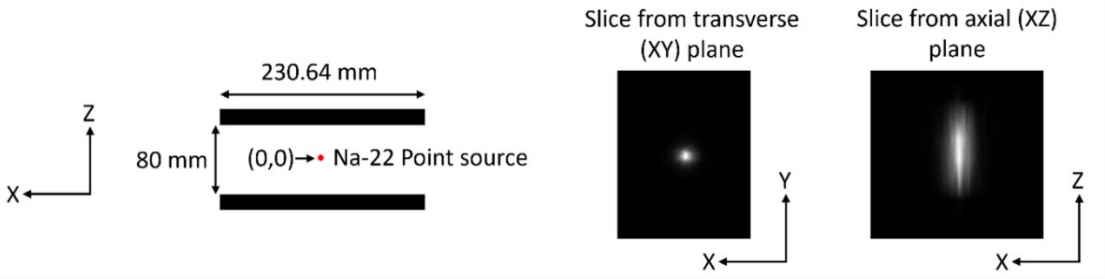

Figure 20. Positioning of the point source in the FOV between the two planar detectors (left). Single slice (2D image) lying in the XY plane of the reconstructed 3D image of the point source (middle). Single slice (2D image) lying in the XZ plane, also called the axial plane.

2.3. Thesis Objectives

The objective of this Thesis research is to advance solid-state PET technology to enable full 3D imaging with planar detector heads. My approach involves rotating the detectors during data

acquisition and increasing the effective angular coverage to achieve fast full 3D acquisition, transforming the planar PET detector technology into a true tomographic organ-targeted PET system. During my Master's degree study, I showed experimentally that this transformation enables accurate reconstruction of tumor volumes, which is essential for quantitative tumor evaluation. Thus, this Thesis lays the foundation for the next generation of organ-targeted PET systems suitable for widespread clinical adoption in screening, diagnostic, and therapeutic settings.

The sections 3 and 4 below contain my research findings. Section 3 presents a manuscript that has been submitted for publication in the Medical Physics journal. This paper discusses my concept of multi-angle acquisition and 3D composite reconstruction using planar organ-targeted PET detectors. Through simulations and experiments, I demonstrate the applicability of this concept to improve brain PET imaging. Section 4 contains a paper that has been accepted for presentation at the IEEE NSS MIC RTSD 2024 conference. This paper discusses optimization of the multi-angle imaging method described in the previous manuscript. The original submission has been revised to eliminate redundant background information on planar PET detector technology, as well as the data acquisition and reconstruction methodologies that were thoroughly covered in the manuscript.

3. Multi-Angle Acquisition and 3D Composite Reconstruction for Brain Imaging Using Planar Organ-Targeted PET Detectors

Anirudh Shahi[1], Harutyun Poladyan[1], Edward Anashkin[2], Borys Komarov[2], Madeline Rapley[1], Alexey Babich[2], Oleksandr Bubon[1,2], Alla Reznik[1,3]

Institutional Affiliations:

1. Department of Physics, Lakehead University, Thunder Bay, ON, Canada
2. Radialis Inc., Thunder Bay, ON, Canada
3. Thunder Bay Regional Health Research Institute, Thunder Bay, Ontario, Canada

Contact information for the corresponding author:

- Email: ashahi2@lakeheadu.ca
- Postal Address: 290 Munro Street, Suite 1300, Thunder Bay, Ontario, Thunder Bay, ON P7A 7T1

Anirudh is the first author.

The following section presents the manuscript that has been submitted for publication in the Medical Physics journal with Anirudh Shahi as its first author. The manuscript evaluates the multi-angle imaging method using simulated, custom-made, and the NEMA NU4-2008 Image Quality phantom. The image reconstruction process is outlined, and the 3D reconstructed images are analyzed both qualitatively and quantitatively.

3.1. Abstract

Background: This study introduces a multi-angle acquisition method aimed at improving image quality in organ-targeted Positron Emission Tomography (PET) with planar detectors. Organ-targeted PET technologies have emerged to address the limitations of conventional whole-body (WB) PET/CT systems, such as restricted axial field-of-view (AFOV), limited spatial resolution, and high radiation exposure associated with PET procedures. The AFOV in organ-targeted PET can be adjusted to the organ of interest, minimizing unwanted signals from other parts of the body, thus improving signal collection efficiency and reducing the dose of radiotracer administered. However, while planar detector PET technology allows for quasi-3D image reconstruction due to the separation between detector heads, it suffers from degraded axial spatial resolution and, consequently, reduced recovery coefficients (RCs) along the axial direction perpendicular to the detectors.

Purpose: The purpose of this study was to evaluate the concept of multi-angle image acquisition with two planar PET detectors and composite full 3D image reconstruction. This leverages data collection from multiple polar angles to enhance contrast recovery in the direction perpendicular to the detector heads. In such, the concept allows to overcome the intrinsic limitations of planar detectors in axial resolution.

Methods: This study evaluates the improvement in the quality of images acquired with the Radialis organ-targeted PET camera through multi-angle image acquisition, in both experimental and simulated imaging scenarios. This includes the use of custom-made phantom with fillable spherical hot inserts, the NEMA NU4-2008 Image Quality (IQ) phantom, and simulations with a digital brain phantom. The analysis involves the comparison of line profiles drawn through the spherical hot inserts, image uniformity, recovery coefficients, and the reduction of smearing observed in the axial planes with and without the multi-angle acquisition strategy.

Results: Significant improvements were observed in reducing smearing, enhancing image uniformity, and increasing recovery coefficients using the evaluated multi-angle acquisition method. In the composite images, the hot spheres appear more symmetrical in all planes. The image uniformity, calculated from the IQ phantom, improves from 7.79%

and 10.98%, as measured in the images from the individual acquisitions, to 2.72% in the composite image. There is also an overall improvement in the RCs as measured from the hot rods of the IQ phantom. Furthermore, the simulation study using the digital human brain phantom demonstrates minimal smearing in the four-angle scan, as opposed to a two-angle scan.

Conclusions: The multi-angle acquisition method offers a promising approach to transform planar PET detector technology into a true tomographic organ-targeted PET system and to enable improvement in image quality while preserving a versatility inherent to planar detector technology. Future research will focus on optimizing the multi-angle imaging protocol, including adjustments to detector separations, number of acquisition angles, and reconstruction iterations, alongside incorporating time-of-flight and reconstruction the point spread function (PSF) modeling to further improve image quality.

3.2. Background

The current trend in PET (Positron Emission Tomography) technology involves tailoring the scan length and local scan duration to suit the specific requirements of the imaging task at hand, including the emerging concept of Total Body (TB) PET. TB-PET imaging represents a significant advancement in PET technology, expanding the axial field of view (AFOV) to encompass the entire patient body during image acquisition[20,30,42,43]. TB-PET systems with an axial length in a range from 1.2 to 2 meters maximize the solid angle coverage, thereby boosting the detection efficiency of coincidence lines of response (LORs). This results in up to 40-fold more events collected vs the WB-PET scanner[43]. Consequently, TB-PET allows for a substantial reduction in the injected dose of a radiotracer and/or acquisition time, minimizing patient motion and discomfort while improving throughput. However, TB-PET scanners come with a higher cost due to up to tenfold increase in the number of individual detector elements compared to conventional whole-body (WB) PET, posing a challenge to clinical adoption; compared to a 20 cm WB-PET detector, a total body PET detector with 100 cm and 200 cm axial lengths will result in 4 and 7.7 times higher component costs[42].

It should be noted that there is a growing range of clinical applications where the focus is not on imaging the entire body but rather on specific organs such as the breast and brain[21,44,45,46]. In such cases, there is no need to surround the patient with extensive detector elements; instead, the emphasis is on enhancing the solid angle coverage of the targeted organ. This approach has the potential to yield superior image quality for specific organs while also offering the option to reduce radiation doses or shorten acquisition times – all at a reduced cost associated with PET imaging.

There are two primary concepts for organ-targeted PET scanners. One concept utilizes two planar detectors positioned on either side of the organ of interest, primarily employed for breast cancer imaging[47]. With a certain (organ-tailored) separation of detector heads during image acquisition, organ-targeted PET can conduct limited-angle tomographic scans and reconstruct quasi-3D images. However, due to limitations in angular coverage, spatial resolution in the direction perpendicular to the detector heads deteriorates, impacting the contrast recovery and overall image quality[48,49,50].

The other concept involves full-ring detectors[31,51]. Generally, ring detector architecture offers more isotropic spatial resolution compared to limited-angle tomography with planar detectors. Nonetheless, planar organ-targeted detectors with adjustable separation and rotation provide flexibility in optimizing the axial field-of-view (AFOV) for imaging various body parts, thereby enhancing clinical utility of organ-targeted PET.

In this study, we assess a method for 3D image reconstruction using data acquired at different angles with planar PET detectors, termed multi-angle image acquisition. Specifically, the detector heads are rotated to collect data from multiple polar angles and to reconstruct images using the combined data set. When paired with a sufficient AFOV to enable fine slice reconstruction, adequate contrast recovery in all three directions can be achieved in the composite image.

Using a clinical planar organ-targeted PET system, called Radialis PET camera, shown in Figure 21a., we conduct one- and two-angle acquisitions of spherical fillable phantoms and a NEMA NU4-2008 Image Quality (IQ) phantom. Our assessment includes evaluating the line profiles, image uniformity, and recovery coefficients in all planes for the one- and two-angle acquisitions.

Figure 21. A) Configuration of the Radialis organ-targeted PET with two planar detector heads. This rotation enables the acquisition of images of the breast in craniocaudal (CC) and mediolateral oblique (MLO) views. B) Schematic of a brain image acquisition with flexibility for the detector heads to be rotated from -90° to +90° around the head as well as at any angle in between.

Additionally, we employ a digital brain phantom to assess the image quality achievable with a planar organ-targeted PET detector using optimized multi-angle acquisition. Although time-of-flight (TOF) and reconstruction PSF modeling are not tested in this study, we anticipate that incorporating this information with multi-angle acquisition will mitigate limited-angle artifacts in planar PET detectors.

3.3. Methods

3.3.1. System description

The Radialis PET organ-targeted camera comprises two planar detectors measuring 172×232 mm similar to that of digital mammography[48,52]. Due to this resemblance, it is also referred to as Positron Emission Mammography, or PEM. The sensor area provides a sufficient AFOV to cover the entire breast reflecting the enlarged solid angle coverage of TB-PET (Figure 21a).

For breast imaging, patients are scanned in a sitting position with the detector heads placed on both sides of slightly compressed (immobilised) breast (Figure 21a)[53]. The detector heads are mounted on a rotational ring mechanism, enabling the acquisition of images in craniocaudal (CC) and mediolateral oblique (MLO) views.

A schematic of a brain image acquisition is shown in Figure 21b. A larger detector separation is used for brain imaging compared to breast imaging. A rotational ring gantry provides the flexibility for the detector heads to be rotated around patient's head between -90° and +90°.

The Radialis organ-targeted PET camera was tested with a large set of standardised and custom tests as required for FDA approval[48,52]. The detectors demonstrated an in-plane (XY) spatial resolution of 2.3 ± 0.1 mm and an axial (Z) spatial resolution of 6.8 mm, with a detector separation of 80 mm[49].

3.3.2. Image Reconstruction

The image reconstruction process for this detector, based on a 3D Maximum Likelihood Estimation Maximization (MLEM) algorithm, was enhanced to reconstruct multi-angle datasets, as depicted in Figure 22. These datasets are stored as List Mode Files (LMF), containing coordinate and energy information from each acquisition. LMF data is acquired from arbitrary angles, and coordinates in LMFs are first transformed into the same coordinate system. Each dataset is then assigned an image space with the same size but varying orientations of the planar detectors. In each iteration of the MLEM reconstruction, line-of-responses (LORs) are projected for each dataset and summed to obtain the composite image. This composite image seeds the image space for the next iteration. The number of MLEM iterations was set to 15 for all reconstructions in this study and a median root prior filter is applied within the MLEM reconstruction after each iteration. It should be noted that a LOR angle-allowance filter is implemented to reject events within the list-mode data based on the endpoints of each LOR[48].

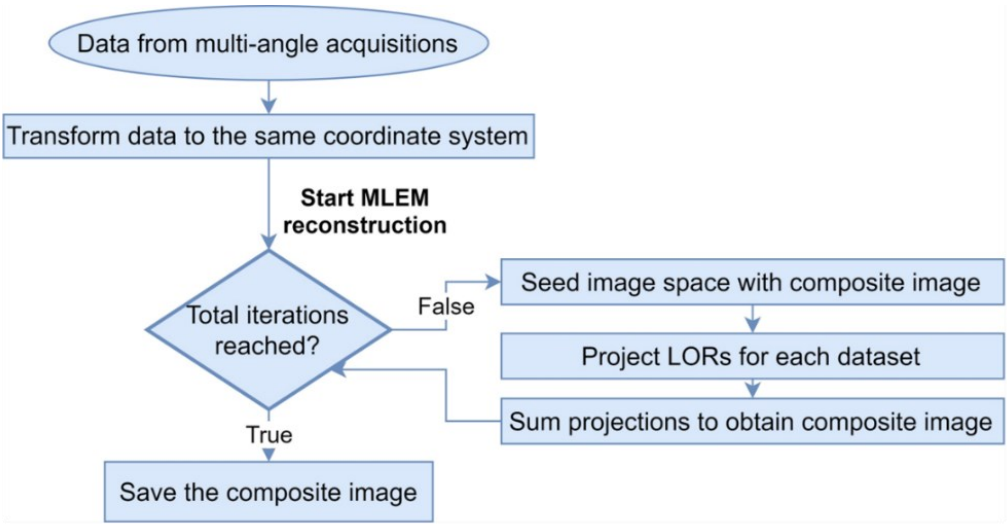

Figure 22. Schematic of the multi-angle MLEM reconstruction method.

3.3.3. Phantom Imaging

A custom-made phantom utilizing a container with separate fillable spheres, was used to assess improvements in lesion size estimation with the multi-angle acquisition method. The phantom consists of four spheres of different diameters (5-, 6.2-, 7.9-, and 12.4-mm), as shown in Figure 23a. The spheres were filled with equal activity concentrations of 18F-Fluorodeoxyglucose (18F-FDG) and were placed in the FOV, as shown in Figure 23b. Then, a two-angle acquisition was performed: first the detectors were oriented at 0°, parallel to the XY plane with 350 mm separation, and then rotated by 90° to be parallel to the YZ plane with 258 mm separation, as illustrated in Figure 23b.

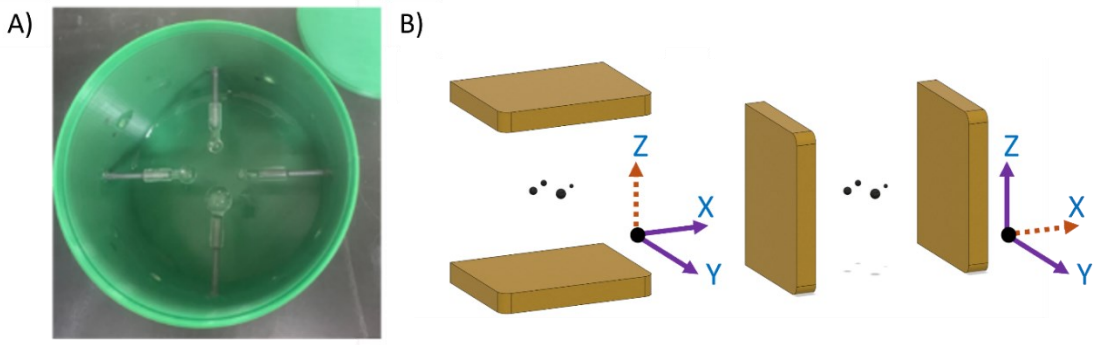

Figure 23. A) Custom-made phantom with separate fillable hot spheres and B) illustration of the two-angle acquisition of the spheres with the detectors oriented 0° and 90°, respectively. The coordinate systems for the images are displayed on the right. The solid, purple, arrows define the transaxial plane for each acquisition. The dotted, orange, arrows are normal to the detector surfaces and indicate the low-resolution axis for each scan.

A standard NEMA Image Quality (IQ) phantom was used to quantify improvements in the recovery coefficient with the multi-angle acquisition method, Figure 24a. The IQ phantom consists of two regions: a solid part with five fillable rods of different diameters (5-, 4-, 3-, 2-, and 1-mm) to determine the activity recovery coefficients and a fillable chamber to assess the image uniformity, using the analysis method we described in a previous study[52]. The IQ phantom was filled with 18F-FDG, oriented along the y axis in the FOV, and then the two-angle acquisitions were performed as shown in Figure 24b.

Approximately 25 million events were acquired per angle in both experiments, namely, with the custom-phantom with fillable spheres and the IQ phantom. The images from the 0° and 90° acquisitions were first reconstructed individually and subsequently fused together using the multi-angle reconstruction method, as described section 3.3.2. For all reconstructions, including both individual 0° and 90° acquisitions and the composite, the image space measured 258 mm×216 mm×350 mm, comprising 322× 216× 438 voxels with cubic voxels of length 0.8 mm. The 3D images were resliced along the Z, X, and Y axes to assess the image quality in the XY, YZ, and XZ planes, respectively.

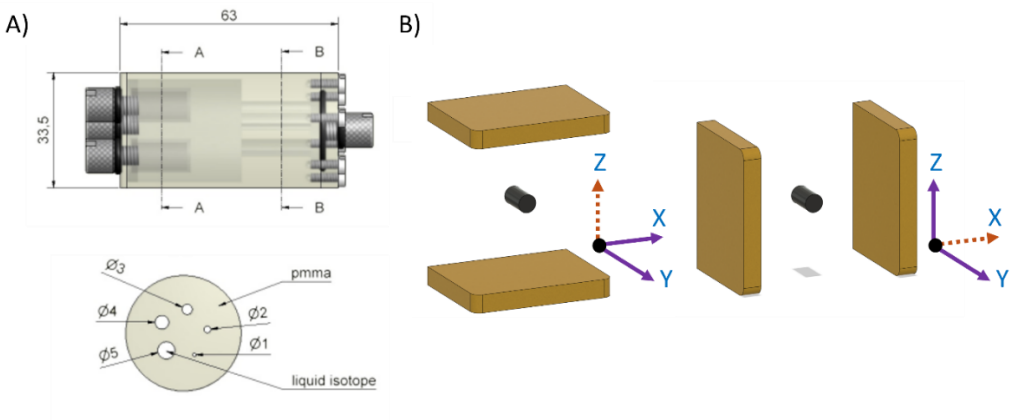

Figure 24. A) Schematic of the NEMA NU-4 Image Quality phantom with the side-view (top) and a cross section view of the hot rods (bottom), source: https://www.qrm.de/en/products/micro-pet-iq-phantom. B) Illustration of the two-angle acquisition of the image quality phantom. The solid, purple, arrows define the transaxial plane for each acquisition. The dotted, orange, arrows are normal to the detector surfaces and indicate the low-resolution axis for each scan.

3.3.4. Digital brain phantom imaging

Simulations were conducted with three sets of tomographic scans, comprising 2, 4, and 6-angle acquisitions, using a digital 18F-FDG PET brain phantom for planar PET detectors similar to the Radialis PET detectors[54]. Total of 10 million events were acquired for each set (as this number of events is expected to be acquired for low dose head scans with the Radialis organ-targeted PET camera), with 5, 2.5, and 1.67 million events per angle for the 2, 4, and 6-angle acquisitions, respectively. The rotation angle increment for each set were 90°, 45°, and 30° for 2, 4, and 6-angle acquisitions, respectively. Simulated separation of the detector heads is 230 mm with the phantom positioned in the middle. As an example, the detector orientations and head positioning for the 4-angle scan is illustrated in Figure 25., with the patient's head facing upwards.

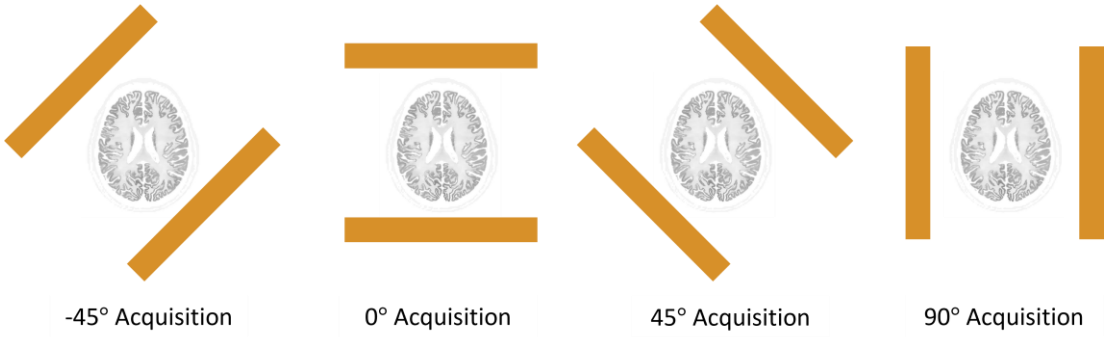

Figure 25. Illustrations of the simulated 4-angle acquisition of the digital brain phantom.

LMF data was simulated by forward projecting from the voxelized digital phantom to the detectors. These simulated LMF datasets were subsequently processed using multi-angle reconstruction, as described in section 2.2, to generate composite images, consisting of 577×433×577 cubic voxels with a length of 0.4 mm.

3.4. Results

3.4.1. Custom-made phantom with four separate hot spheres

Figure 26. compares selected slices from the 3D images of the hot spheres reconstructed individually for the 0° and 90° scans (rows a-b) and using the composite reconstruction method (row c). In the individually reconstructed images, we observe that the spheres are undistorted in slices lying on the transaxial planes, which are parallel to the detectors. However, the spheres are smeared along the axis normal to the detector heads, which is the z and x axis for the 0° and 90° scans, respectively, as indicated by the dotted, orange, arrows in Figure 23b. The smearing is significantly reduced in the composite image, in which the spheres appear more symmetrical in all planes, Figure 26 (row c).

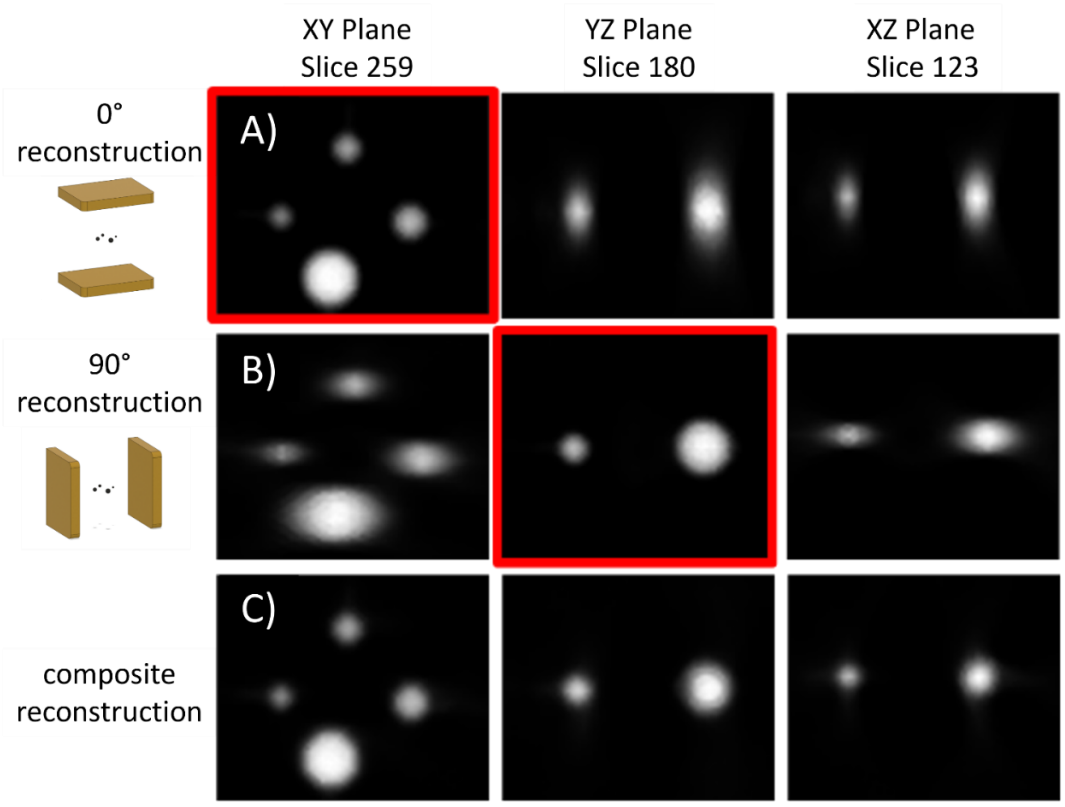

Figure 26. Selected slices from the 3D images of the custom-made phantom with four separate spheres. Rows A)-B) correspond to images reconstructed individually for the 0° and 90° scans and row C) corresponds to composite images generated using the multi-angle reconstruction method. The first, second, and third columns show selected slices from the XY, YZ, and XZ planes of the 3D images, respectively. The left column shows all four spheres in the FOV, the second column shows the 6.2 mm and 12.4 spheres, and the third column shows the 5 mm and 7.9 mm spheres. The slices highlighted in red correspond to the high-resolution planes of the detector in each orientation.

We also assessed the reconstructed images using line profiles drawn through the maximum intensity voxels of each hot sphere. Figure 27. shows normalized line profiles through all spheres along the x, y, and z axis. As expected, the line profiles are considerably broader along the z axis in the 0° acquisition compared to x and y axis due to degraded spatial resolution along the z axis, which is normal to the detectors. Similarly, the line profiles are broad along the x axis in the 90° acquisition compared to

the y and z axis. The variance between the line profiles reduces along all three axes of the composite image, indicating more accurate representation of activity distribution in the spheres.

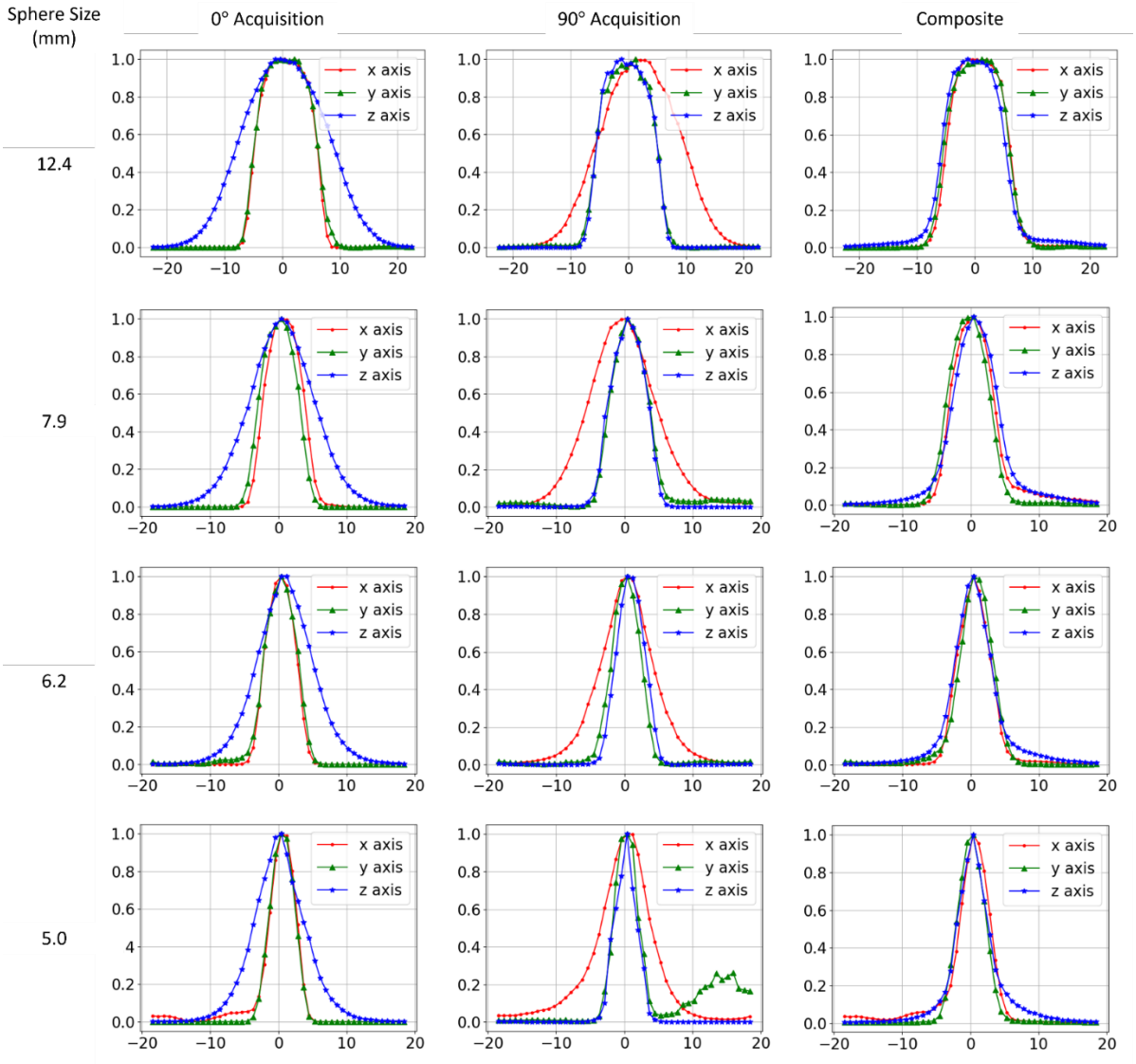

Figure 27. Line profiles drawn across the 12.4, 7.9, 6.2, and 5 mm spheres along all three axes in the 3D images obtained from 0°, 90°, and composite reconstructions. In each plot, the vertical axis corresponds to the normalize pixel intensity and the horizontal axis corresponds to distance, in mm, from the center of each sphere.

3.4.2. NEMA NU4 Image Quality phantom

Figure 28. shows selected slices from the individually reconstructed and composite images of the IQ phantom. The phantom details are well visualized in the slices parallel to the transaxial planes, which are XY and YZ for the 0° and 90° scans, respectively. As expected, there is smearing along the axes normal to the detectors, which also results in poor image quality and inability to reconstruct activity in the hot rods due to a significant signal spill-over. Also, slice 85 in the XZ plane from the 90° reconstruction shows how smearing results in overlap of the 5 and 4 mm rods.

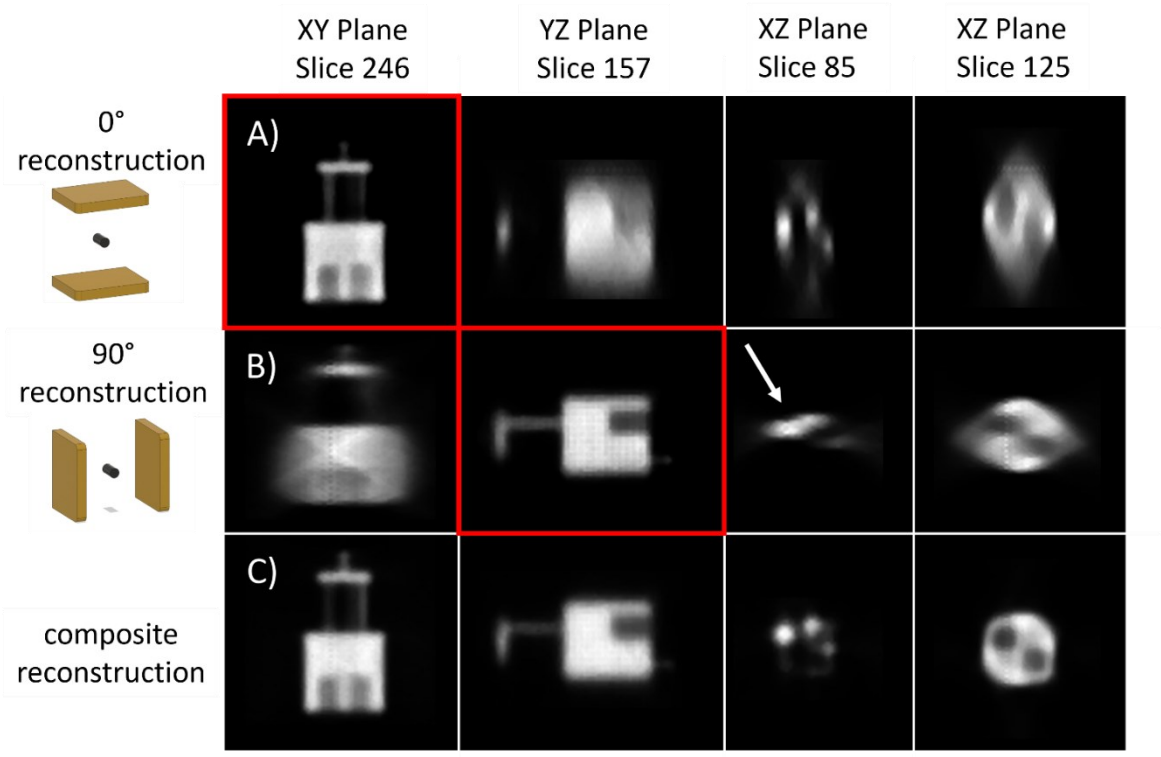

Figure 28. Selected slices from the 3D images of the IQ phantom. Rows A)-B) correspond to images reconstructed individually for the 0° and 90° scans and row C) corresponds to composite images generated using the multi-angle reconstruction method. The first column shows single slices from the XY plane of the 3D images, the second column shows single slices from the XZ plane, and the last two columns show single slices from the YZ plane. The slices highlighted in red correspond to the high-resolution planes of the detector in each orientation.

Figure 29. shows line profiles drawn through the cold chambers, from slice 125, of the individual and composite reconstructions. The line profiles are drawn to compare the contrast in activity inside and outside the cold chambers for the individual and composite reconstructions. The valleys in the line profile correspond to centers of the cold chambers (15 mm center-to-center) and the peaks correspond to regions in the hot background. In the composite reconstruction, there is an improved contrast in intensities of the peaks and valleys as compared to the individual reconstructions. This indicates improved image contrast between the cold chambers and the hot background and reduced spillover of activity from smearing.

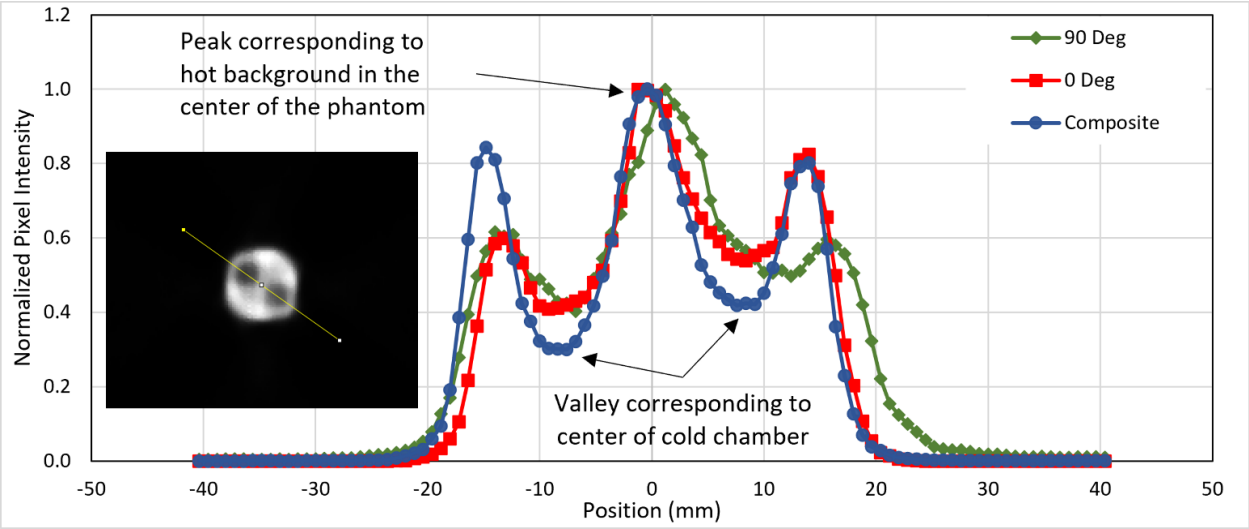

Figure 29. Normalized line profiles through the cold chambers in the 0°, 90°, and composite reconstructions. Example of the line profile drawn through the cold chambers in the composite image is also shown on the plot.

3.4.3. Quantitative image quality analysis

Uniformity derived as a standard deviation from the mean grey value in the uniform region of the IQ phantom is 7.79% and 10.98 % for the 0° and 90° reconstructions, respectively. The standard deviation, of 2.72%, is significantly lower in the composite image which indicates improvement in image uniformity.

The recovery coefficients (RCs) for the 0°, 90°, and composite reconstructions were measured in slices parallel to the XZ plane and are shown in Figure 30. There is variation in the RCs between the two 0° and 90° acquisitions. However, for all three rods, there is an overall improvement in RCs in the composite image.

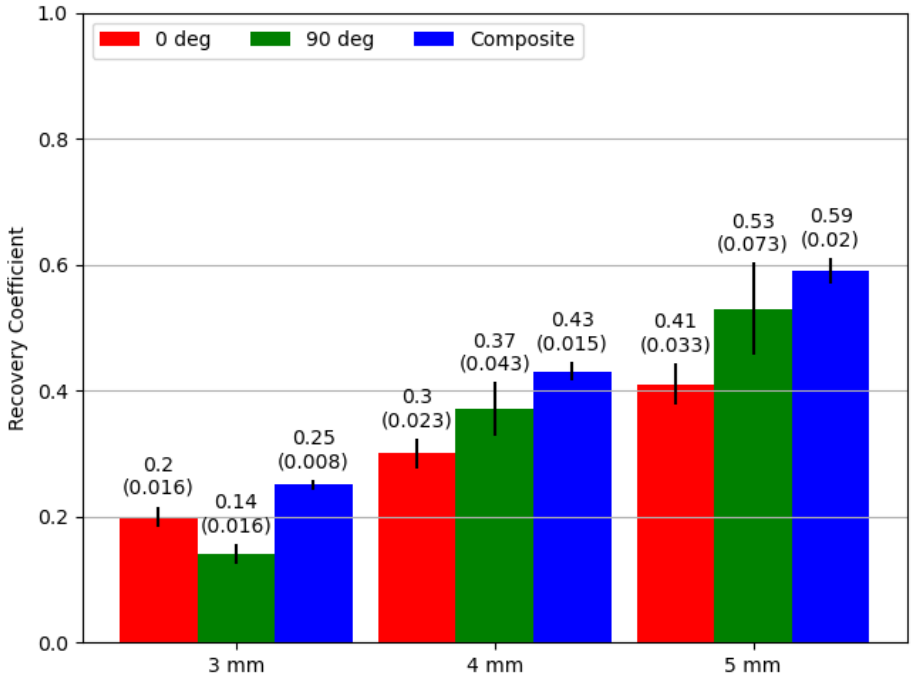

Figure 30. Recovery coefficients calculated for the 0°, 90° and the composite reconstruction.

3.4.4. Simulated brain imaging with digital human brain phantom

Figure 31. presents slices of the reconstructed composite images from simulated multi-angle acquisitions of the digital human brain phantom. No significant geometric distortions are observed in the sagittal and coronal planes of the 2-angle scan. However, the axial (low-resolution) detector plane in the 2-angle scan exhibits smearing in the composite image. This diagonal smearing occurs due to missing projections between the 0° and 90° scans. The smearing is significantly reduced in the 4-angle scan, which involves two additional rotations (45° and 135°) of the detectors to acquire the missing

projections. Moreover, no significant qualitative difference was observed in the images between the 6-angle scan and the 4-angle scan.

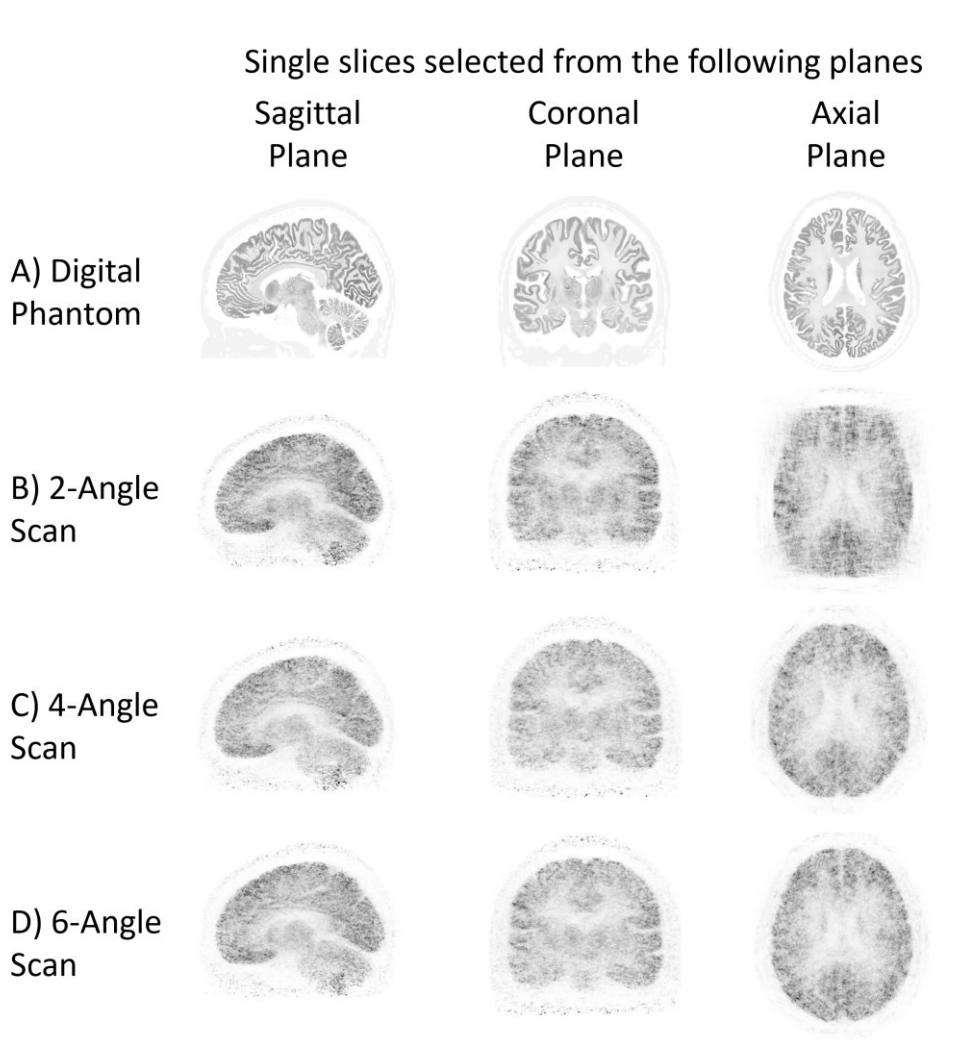

Figure 31. A) Axial, coronal, and sagittal views of the digital brain phantom. B)-D) selected slices from the 3D composite images from the simulated 2-, 4-, and 6-angle acquisitions of the phantom.

3.5. Discussion

In this work we performed a set of tests to investigate the feasibility of 3D tomographic imaging using the Radialis organ-targeted PET camera with planar detector heads. In

previous studies, we characterized its performance and determined that the scanner had a significantly higher geometric sensitivity and count rate performance compared to WB-PET systems[48]. Although single-angle image acquisition allows quasi-3D image reconstruction, the axial spatial resolution (i.e., in the direction perpendicular to the detector heads) degrades and the smearing arise largely due to limited angular view.

In this study, we evaluated the impact of the multi-angle reconstruction technique on the image quality of a planar organ-targeted PET camera. We observed significant improvements in overall image quality of both, a phantom featuring hot spheres and the NEMA NU4 IQ phantom, following a two-angle acquisition. We demonstrated that the incorporation of two angle acquisitions in the scanning protocol of a planar PET camera can result in a more accurate representation of objects, such as the hot rods (3- mm) and cold chambers (8 mm diameter) of the IQ phantom, in the axial planes. The two-angle acquisition also resulted in a higher image uniformity, which is indicative of an improved signal-to-noise ratio and may partly be due to a higher total number of events in the composite image. Although some smearing is observed on the outer edges of the cold chambers in the composite image, we anticipate that collecting additional angular data will further reduce this artifact.

We also observed an improvement in the RC values indicating enhanced quantitative accuracy with a two-angle acquisition. For example, for the 5-mm rod, the RC was measured to be 0.41 and 0.53 in the images reconstructed from 0° and 90° angles and 0.59 in the composite reconstruction. It should be noted that relatively low RC values are due to a particular phantom orientation so that its cylindrical axis is parallel to the detectors in both the 0° and 90° acquisitions. This orientation results in RC measurements in planes where smearing occurs[50,55] thus allowing for an efficient illustration of the RCs improvements in composite images.

The phantom experiments also demonstrated that additional rotations are needed to optimize the multi-angle imaging protocol because there remain missing projections between the 0° and 90° acquisitions which contribute to image distortion. In fact, our simulations of a digital brain phantom demonstrated much better visualization of brain features and a reduction in smearing, especially following the 4-angle reconstruction. So,

as a next step we will perform phantom experiments with greater number of detector rotations, which may also lead to further improvements of contrast recovery.

An advantage of the organ-targeted 3D PET system, consisting of a pair of planar detectors, lies in its versatility in imaging applications compared to traditional approach to organ-targeted PET systems dedicated and optimized for only imaging a particular organ (such as brain or breast). Possible dynamic adjustments in detector separations to ensure optimal solid-angle coverage of the specific organ under investigation improves geometric sensitivity and allows for low dose PET imaging for a variety of medical conditions thus improving clinical utility of organ-targeted PET. While for specific organs, like breast, single projection image acquisitions (in CC and MLO view) are sufficient[53], diagnostic potential of imaging organs like brain will be significantly improved with multi-angle image acquisition due to reduced smearing in the direction perpendicular to the detectors. Additionally, given the high sensitivity of the Radialis organ-targeted PET camera, the acquisition time per angle is expected not to exceed 5 minutes for the lowest activity of an injected radiotracer. Thus, the multi-angle acquisition approach is not expected to impact the patient's throughput.

3.6. Conclusions

We have shown that rotating planar PET detectors offers a practical solution to achieve high-resolution 3D tomographic imaging with planar organ-targeted PET detectors. We measured improvements in image quality, including better image uniformity, recovery coefficients, and demonstrated reduced smearing following multi-angle acquisition and 3D composite image reconstruction. In the future, we will optimize the number of acquisition angles and reconstruction iterations to enhance the image quality for the multi-angle data acquisition and composite image reconstruction. We expect that integrating TOF reconstruction and PSF modelling in the image reconstruction workflow will further improve the image quality.

3.7. Acknowledgements

The authors gratefully acknowledge financial support from Natural Sciences and Engineering Research Council of Canada Discovery and Alliance programs, MITACS IT30395, Ontario Research Fund: Research Excellence, Terry Fox Foundation and

Research Institute, Ontario Institute for Cancer Research, Canadian Research Chairs 2018-00015 and Radialis Inc. The authors also acknowledge Radialis Inc. for providing access to the Radialis clinical organ-targeted PET system used in this work.

4. Optimizing the Multi-Angle Imaging Method for Planar Organ-Targeted PET Detectors

Anirudh Shahi[1], Harutyun Poladyan[1], Edward Anashkin[2], Borys Komarov[2], Henry Maa-Hacquoil[1], Alexey Babich[2], Oleksandr Bubon[1,2], Alla Reznik[1,3]

Institutional Affiliations:

4. Department of Physics, Lakehead University, Thunder Bay, ON, Canada
5. Radialis Inc., Thunder Bay, ON, Canada
6. Thunder Bay Regional Health Research Institute, Thunder Bay, Ontario, Canada

Anirudh is the first author.

The following section presents a paper that has been submitted for presentation at the IEEE NSS MIC RTSD 2024 conference, with Anirudh Shahi as the first author. This paper discusses optimization of the multi-angle imaging method described in the previous manuscript. The original submission has been revised to eliminate redundant background information on planar PET detector technology, as well as the data acquisition and reconstruction methodologies that were thoroughly covered in the manuscript.

4.1. Abstract

Organ-targeted PET systems, with two planar detector heads, can allow dynamic adjustment of detector separation and rotation, enabling the optimization of the solid angle coverage of several organs-of-interest and applications in image-guided biopsy. However, planar PET detectors suffer from a low axial spatial resolution, due to a limited angular view, which results in severe smearing of objects along the axial plane. Previously, we outlined a multi-angle imaging method, for collecting missing projections, which resulted in both a reduction in smearing of objects and improvements in the recovery coefficient. Here, we determine the number of acquisition angles and image reconstruction iterations that produce optimal image quality using the multi-angle image method for a 300 mm separation of the detector heads. For quantitative analysis, we use the NEMA NU4 2008 standard image quality phantom, filled with 18F-FDG, in the experiments. Our results indicate that performing a 4-angle scan, with 45° increment rotations of the detector heads, provides optimal image quality with an image uniformity of 6.29%, recovery coefficients of 0.15, 0.33, 0.52, and 0.73 for the 2-, 3-, 4-, and 5-mm rods, and spill-over ratios of 0.23 and 0.18 for the air and water chambers, respectively. We also determined that increasing the number of image reconstruction iterations results in minimal spill-over of activity inside the air and water chambers. The multi-angle imaging method is not expected to impact the patient throughput since we observed an improved image quality using the same scan duration time in the 4-angle composite image compared to the standard 1-angle image.

4.2. Introduction

Planar PET detectors have a limited angular view, which significantly degrades the spatial resolution along the z-axis and degrades the image quality in the axial planes[48,56,57]. While methods such as resolution modelling and implementing time-of-flight reconstruction have been explored for overcoming challenges with limited angular view, we previously evaluated the image quality following tomographic scans of phantoms[56,57]. Figure 32. shows how increasing the detector rotation optimizes the angular view and allows the collection of missing projections. In this figure, an average sized human brain is placed between the detector heads and the detectors are placed 300

mm apart. A 2-angle acquisition greatly increases the angular view, but missing projections remain. A 4-angle acquisition maximizes the available projections and further rotations of the detector heads will not provide additional information for improvements in image reconstruction.

We have outlined a multi-angle imaging method for collecting the missing projections previously. We conducted 2-angle scans and demonstrated a reduction in smearing of objects and improvements in the recovery coefficient in the composite image. In this work, we optimize the multi-angle reconstruction for reconstructing data from tomographic scans in planar PET detectors. We use a clinical planar organ- targeted PET system to determine the optimal number of angles and image reconstruction iterations used in the multi-angle imaging method. We perform 1-, 2-, 4-, and 6-angle scans of an image quality phantom and evaluate 15 and 50 iterations for image reconstruction.

Figure 32. Schematic, to scale, of detector orientations during a multi-angle head scan with planar organ-targeted PET detectors of the same size as the Radialis Camera detectors and a separation of 300 mm. A) 1-angle scan with detectors oriented 0°, B) 2-ange scan with detectors rotated by 90°, C) 4-angle scan with detectors incrementally rotated by 45°.

4.3. Materials & Methods

The separation between the two planar detectors of the Radialis PET camera was set to 300 mm for all experiments in this study. A NEMA NU4 2008 image quality phantom was used to quantify the improvements in the recovery coefficient with the multi-angle

acquisition method[52]. The image quality phantom was filled with 3.82 MBq of 18F-FDG, with its axis of symmetry parallel to the detectors, as shown in Figure 33.

Four sets of scans were performed, each with a different total number of detector rotations. First, a 1-angle scan was performed with the detectors oriented at 0°. Next, 2-angle scan was performed with the detectors oriented at 90°. Finally, 4- and 6-angle scans were performed with the detectors rotated incrementally by steps of 45° and 30°, respectively. The total time for each 1-, 2-, 4-, and 6-angle scan was set to 5 min. For each scan, the total time of 5 min was evenly divided for each angle acquisition.

A composite reconstruction employing a 3D MLEM algorithm was utilized to reconstruct multi-angle datasets. The image space consisted of 375×216×375 cubic voxels with a length of 0.8 mm. By default, in clinic, 15 iterations are used during image reconstruction for the Radialis PET camera. Here, we first reconstruct the 1-, 2-, 4-, and 6-angle scans using the default 15 iterations and then we choose the 4-angle scan to evaluate the image quality with 15 iterations and 50 iterations of the reconstruction.

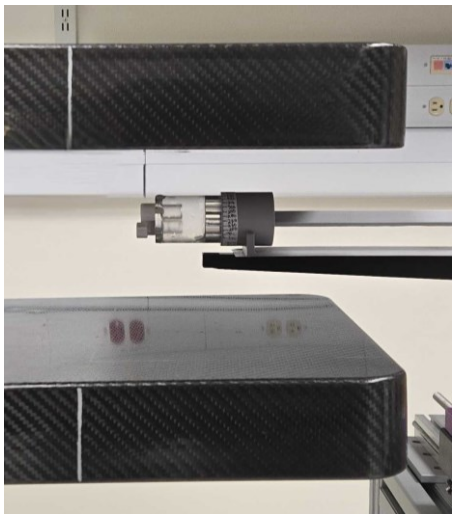

Figure 33. Illustration of the image quality phantom positioning inside the Radialis Camera for the multi-angle acquisitions.

4.4. Results

Figure 34. shows single slices from the axial plane of the reconstructed 3D composite images, using 15 iterations, following the multi-angle acquisitions. The image quality is

poor from the 1-angle scan due to a low axial spatial resolution which results in smearing of the image quality phantom. The smearing reduces significantly following the 2-angle scan, resulting in an improvement in the shape of all three regions and a good separation of the two cold chambers. The 4-angle scan results in a more circular shape of the small animal phantom compared to the 2-angle acquisition. There is no significant qualitative improvement following the 6-angle acquisition.

The quantitative measurements obtained from the 3D composite images following the multi-angle acquisitions are shown in Table 6. There is a significant improvement in the uniformity and recovery coefficients of 2-angle composite image compared to the 1-angle image. The uniformity and recovery coefficients, for the 4 and 5 mm rods, further improve in the 4-angle composite image but no significant quantitative improvement in the 6-angle composite image.

A comparison of the composite images reconstructed with 15 and 50 iterations is provided in Figure 35. using data from the 4-angle scan. The time to reconstruct the composite images for the 15 and 50 iterations was 715s and 2280s, respectively. Increasing the number of iterations results in an improvement of spill over in the cold chambers which is also evident from the quantitative improvement in the SOR as measured in the images reconstructed using 50 iterations as compared to 15 iterations, Table 7. There is no significant difference in the uniformity and contrast recovery of the hot rods in the composite image reconstructed with 15 and 50 iterations.

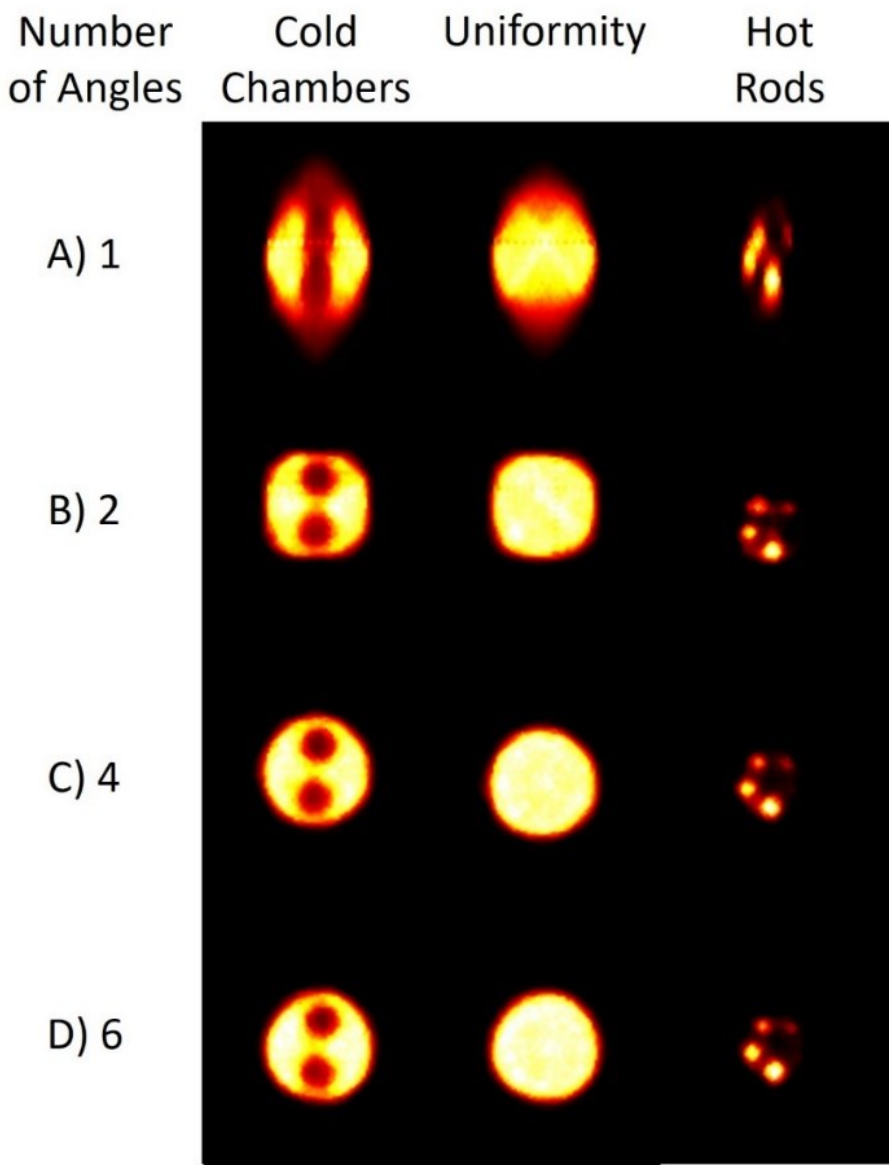

Figure 34. Single slices of the 3D composite images reconstructed from the 1-, 2-, 4-, and 6-angle scans of the image quality phantom. The slices correspond to the axial plane of the 3D images and illustrate the image quality of the three chambers in the small animal phantom following the multi-angle acquisitions.

Table 6. Calculated uniformity, recovery coefficients, and spill over ratios from the composite images following the multi-angle acquisitions.							
Number of Angles	Uniformity (%)	Recovery Coefficient (% std)				Spill Over Ratio (%std)	
		2 mm	3 mm	4 mm	5 mm	Air Chamber	Water Chamber
1	18.24	-	0.3 (19)	0.36 (19)	0.40 (18)	0.25 (19)	0.21 (19)
2	8.07	0.14 (12)	0.36 (9)	0.45 (9)	0.64 (10)	0.26 (10)	0.41 (20)
4	6.29	0.15 (10)	0.33 (6)	0.52 (7)	0.73 (7)	0.23 (8)	0.18 (7)
6	5.99	0.14 (11)	0.34 (8)	0.55 (6)	0.67 (7)	0.24 (10)	0.18 (10)

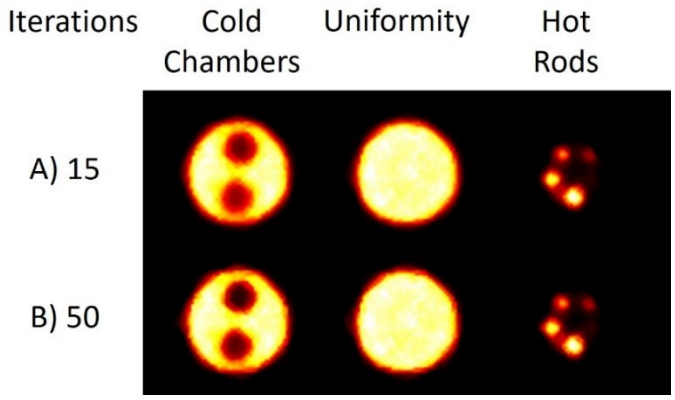

Figure 35. Single slices of the 3D images reconstructed from the 4-angle scan of the image quality phantom. The slices correspond to the axial plane of the 3D images and illustrate the image quality of the three chambers in the image quality phantom following reconstruction with A) 15 iterations and B) 50 iterations.

Table 7. Calculated spill over ratios from the composite images reconstructed with 15 and 50 iterations following the 4-angle scan of the image quality phantom.	
Number of Iterations	Spill Over Ratio (% std)

	Air Chamber	Water Chamber
15	0.23 (8)	0.18 (7)
50	0.16 (8)	0.09 (8)

4.5. Conclusion

The goal of this work was to optimize the number of angles and iterations used in the multi-angle imaging method for a planar organ targeted PET detector. We perform 1-, 2-, 4-, and 6-angle scans of the NEMA NU4 2008 image quality phantom. The total time for each set of scans is 5 mins. A standard, 1-angle, scan results in a uniformity of 18.25%, recovery coefficient of 0.40 for the 5 mm hot rod, and spill over ratios of 0.25 and 0.21 for the air and water chambers, respectively. We determined that a 4-angle scan, with the planar detectors rotated incrementally by steps of 45°, results in optimal uniformity of 6.29%, recovery coefficient of 0.73 for the 5 mm hot rod, and spill over ratios of 0.23 and 0.18 for the air and water chambers, respectively. The 4-angle scan also produces composite image with the most accurate shape of the image quality phantom. Furthermore, we also determined that increasing the number of reconstruction iterations from 15 to 50 results in a significant improvement of the spill over, as measured in the 4-angle composite image, while having no impact on the uniformity and recovery coefficient.

5. Thesis Summary and Concluding Remarks

This Thesis presents a detailed evaluation of multi-angle imaging with a planar organ-targeted Positron Emission Tomography (PET) detector that was previously developed by our group. The planar organ-targeted PET detector addresses limitations of traditional WB-PET detectors, primarily limited spatial resolution and system sensitivity. Recent clinical trials have demonstrated the potential of this planar PET technology for an improved visualization of cancerous lesions within the breast, even with a dose reduction in comparison with standard WB-PET. Additionally, unlike organ-targeted detectors based on ring geometries, this planar PET detector offers greater versatility by allowing for adjustable separation and rotation of the two flat detector panels, making it suitable for imaging multiple organs of interest.

This research addresses the smearing artifacts observed in planar PET detectors, caused by their limited angular coverage, which leads to degraded 3D reconstructed images and reduced accuracy in activity estimation within small lesions. To overcome this challenge, this thesis outlines and evaluates a multi-angle imaging method, where the detectors are rotated to increase the effective angular coverage of the planar PET detectors.

Experiments were conducted using the Radialis PET camera, a clinical planar organ-targeted PET detector. Tests with standard and custom-made phantoms demonstrated that multi-angle image acquisition and reconstruction significantly reduces smearing in 3D images and improves the accuracy of activity estimation in small objects with the planar PET detector.

This thesis demonstrates that full 3D image reconstruction can be achieved with planar PET technology, such as the Radialis PET camera, originally designed for 2D breast cancer imaging. However, its 3D imaging capabilities are constrained by limited angular coverage. Multi-angle imaging can overcome this limitation, enabling 3D image reconstruction of the brain and improving the quantification of activity inside tumors with planar PET detectors.

6. References

[1] Del Guerra, Alberto, Nicola Belcari, and M. Bisogni. "Positron emission tomography: its 65 years." La Rivista del Nuovo Cimento 39 (2016): 155-223.
[2] Cherry, Simon R., et al. PET: physics, instrumentation, and scanners. Springer New York, 2006.
[3] Conti, Maurizio, and Lars Eriksson. "Physics of pure and non-pure positron emitters for PET: a review and a discussion." EJNMMI physics 3 (2016): 1-17.
[4] Levin, Craig. "Basic physics of radionuclide imaging." Emission tomography. Academic Press, 2004. 53-88.
[5] Kamal, Anwar. Nuclear physics. Springer, 2014.
[6] Saha, Gopal B. Basics of PET Imaging : Physics, Chemistry, and Regulations. Cham, Springer, 2016.
[7] Cherry, S.R., Sorenson, J.A., Phelps, M.E., 2012. Physics in Nuclear Medicine. Elsevier Health Sciences.
[8] Lecomte, Roger. "Novel detector technology for clinical PET." European journal of nuclear medicine and molecular imaging 36 (2009): 69-85.
[9] Lecoq, Paul, and Stefan Gundacker. "SiPM applications in positron emission tomography: toward ultimate PET time-of-flight resolution." The European Physical Journal Plus 136.3 (2021): 292.
[10] Gundacker, Stefan, and Arjan Heering. "The silicon photomultiplier: fundamentals and applications of a modern solid-state photon detector." Physics in Medicine & Biology 65.17 (2020): 17TR01.
[11] Roncali, Emilie, and Simon R. Cherry. "Application of silicon photomultipliers to positron emission tomography." Annals of biomedical engineering 39 (2011): 1358-1377.
[12] Wagatsuma, Kei, et al. "Comparison between new-generation SiPM-based and conventional PMT-based TOF-PET/CT." Physica Medica 42 (2017): 203-210.
[13] Hahn, A., et al. "Direct comparison of SiPM and PMT sensor performances in a large-size imaging air Cherenkov telescope." Nuclear Instruments and Methods in Physics Research Section A: Accelerators, Spectrometers, Detectors and Associated Equipment 1064 (2024): 169350.
[14] Schaart, Dennis R., et al. "LaBr3: Ce and SiPMs for time-of-flight PET: achieving 100 ps coincidence resolving time." Physics in Medicine & Biology 55.7 (2010): N179.
[15] Zatcepin, Artem, and Sibylle I. Ziegler. "Detectors in positron emission tomography." Zeitschrift für Medizinische Physik 33.1 (2023): 4-12.
[16] Majewski, Stanislaw. "The path to the “ideal” brain PET imager: The race is on, the role for TOF PET." Il nuovo cimento C 43.1 (2020): 1-35.
[17] Karlberg, Anna M., et al. "Quantitative comparison of PET performance—Siemens Biograph mCT and mMR." EJNMMI physics 3 (2016): 1-14.
[18] Alanazi, S. F. "Comparison of image quality and standardized uptake values (SUV) of two PET/CT imaging system using F-18 and Ga-68." Journal of Physics: Conference Series. Vol. 2701. No. 1. IOP Publishing, 2024.
[19] Pan, Tinsu, et al. "Performance evaluation of the 5-Ring GE Discovery MI PET/CT system using the national electrical manufacturers association NU 2-2012 Standard." Medical physics 46.7 (2019): 3025-3033.

[20] Vandenberghe, Stefaan, Pawel Moskal, and Joel S. Karp. "State of the art in total body PET." EJNMMI physics 7 (2020): 1-33.
[21] Moliner, Laura, et al. "NEMA performance evaluation of CareMiBrain dedicated brain PET and comparison with the whole-body and dedicated brain PET systems." Scientific reports 9.1 (2019): 15484.
[22] Kapoor, Mayank, and Anup Kasi. "PET scanning." (2020).
[23] Martin, Ole, et al. "PET/MRI versus PET/CT for whole-body staging: results from a single-center observational study on 1,003 sequential examinations." Journal of nuclear medicine 61.8 (2020): 1131-1136.
[24] Tam, Marty C., et al. "Diagnostic accuracy of FDG PET/CT in suspected LVAD infections: a case series, systematic review, and meta-analysis." Cardiovascular Imaging 13.5 (2020): 1191-1202.
[25] Han, Sangwon, and Joon Young Choi. "Impact of 18F-FDG PET, PET/CT, and PET/MRI on staging and management as an initial staging modality in breast cancer: a systematic review and meta-analysis." Clinical nuclear medicine 46.4 (2021): 271-282.
[26] Surti, S., M. E. Werner, and J. S. Karp. "Study of PET scanner designs using clinical metrics to optimize the scanner axial FOV and crystal thickness." Physics in Medicine & Biology 58.12 (2013): 3995.
[27] Surti, Suleman, Austin R. Pantel, and Joel S. Karp. "Total body PET: why, how, what for?." IEEE transactions on radiation and plasma medical sciences 4.3 (2020): 283-292.
[28] Prenosil, George A., et al. "Performance characteristics of the Biograph Vision Quadra PET/CT system with a long axial field of view using the NEMA NU 2-2018 standard." Journal of nuclear medicine 63.3 (2022): 476-484.
[29] Spencer, Benjamin A., et al. "Performance evaluation of the uEXPLORER total-body PET/CT scanner based on NEMA NU 2-2018 with additional tests to characterize PET scanners with a long axial field of view." Journal of Nuclear Medicine 62.6 (2021): 861-870.
[30] Cherry, Simon R., et al. "Total-body PET: maximizing sensitivity to create new opportunities for clinical research and patient care." Journal of Nuclear Medicine 59.1 (2018): 3-12.
[31] Moliner, Laura, et al. "Design and evaluation of the MAMMI dedicated breast PET." Medical physics 39.9 (2012): 5393-5404.
[32] Iriarte, Ana, et al. "System models for PET statistical iterative reconstruction: A review." Computerized Medical Imaging and Graphics 48 (2016): 30-48.
[33] Zhou, Jian, and Jinyi Qi. "Fast and efficient fully 3D PET image reconstruction using sparse system matrix factorization with GPU acceleration." Physics in Medicine & Biology 56.20 (2011): 6739.
[34] Ortuno, J. E., et al. "Efficient methodologies for system matrix modelling in iterative image reconstruction for rotating high-resolution PET." Physics in Medicine & Biology 55.7 (2010): 1833.
[35] Alessio, Adam M et al. “Application and evaluation of a measured spatially variant system model for PET image reconstruction.” IEEE transactions on medical imaging vol. 29,3 (2010): 938-49. doi:10.1109/TMI.2010.2040188
[36] Surti, Suleman, and Joel S. Karp. "Design considerations for a limited angle, dedicated breast, TOF PET scanner." Physics in Medicine & Biology 53.11 (2008): 2911.

[37] Schaart, Dennis R. "Physics and technology of time-of-flight PET detectors." Physics in Medicine & Biology 66.9 (2021): 09TR01.
[38] Chicheportiche, Alexandre, Rami Marciano, and Marina Orevi. "Comparison of NEMA characterizations for Discovery MI and Discovery MI-DR TOF PET/CT systems at different sites and with other commercial PET/CT systems." EJNMMI physics 7 (2020): 1-20.
[39] Razdevšek, Gašper, et al. "Multipanel limited angle PET system with 50 ps FWHM coincidence time resolution: a simulation study." IEEE Transactions on Radiation and Plasma Medical Sciences 6.6 (2021): 721-730.
[40] Baldassi, Brandon, et al. "Image quality evaluation for a clinical organ-targeted PET camera." Frontiers in Oncology 14 (2024): 1268991.
[41] Poladyan, Harutyun, et al. "Gaussian position-weighted center of gravity algorithm for multiplexed readout." Physics in Medicine & Biology 65.16 (2020): 165003.
[42] Pantel, Austin R., David A. Mankoff, and Joel S. Karp. "Total-body PET: will it change science and practice?." Journal of Nuclear Medicine 63.5 (2022): 646-648.
[43] Surti, Suleman, Austin R. Pantel, and Joel S. Karp. "Total body PET: why, how, what for?." IEEE transactions on radiation and plasma medical sciences 4.3 (2020): 283-292.
[44] Miyake, Kanae Kawai, Yuji Nakamoto, and Kaori Togashi. "Current status of dedicated breast PET imaging." Current Radiology Reports 4 (2016): 1-11.
[45] Narayanan, Deepa, and Wendie A. Berg. "Use of breast-specific PET scanners and comparison with MR imaging." Magnetic Resonance Imaging Clinics 26.2 (2018): 265-272.
[46] Hathi, Deep K., et al. "Evaluation of primary breast cancers using dedicated breast PET and whole-body PET." Scientific Reports 10.1 (2020): 21930.
[47] Moliner, Laura, et al. "NEMA performance evaluation of CareMiBrain dedicated brain PET and comparison with the whole-body and dedicated brain PET systems." Scientific reports 9.1 (2019): 15484.
[48] Stiles, Justin, et al. "Evaluation of a high-sensitivity organ-targeted PET camera." Sensors 22.13 (2022): 4678.
[49] Gravel, Paul, Yusheng Li, and Samuel Matej. "Effects of TOF resolution models on edge artifacts in PET reconstruction from limited-angle data." IEEE transactions on radiation and plasma medical sciences 4.5 (2020): 603-612.
[50] Luo, Weidong, Edward Anashkin, and Christopher G. Matthews. "Performance evaluation of a PEM scanner using the NEMA NU 4—2008 small animal PET standards." IEEE Transactions on Nuclear Science 57.1 (2010): 94-103.
[51] García Hernández, Trinitat, et al. "Performance evaluation of a high resolution dedicated breast PET scanner." Medical Physics 43.5 (2016): 2261-2272.
[52] Baldassi, Brandon, et al. "Image quality evaluation for a clinical organ-targeted PET camera." Frontiers in Oncology 14 (2024): 1268991.
[53] Freitas, Vivianne, et al. "Breast cancer detection using a low-dose positron emission digital mammography system." Radiology: Imaging Cancer 6.2 (2024): e230020.
[54] Belzunce, Martin A., and Andrew J. Reader. "ultra high-resolution radiotracer-specific digital pet brain phantoms based on the BigBrain atlas." Medical Physics 47.8 (2020): 3356-3362.
[55] Matej, Samuel, et al. "Image-based modeling of PSF deformation with application to limited angle PET data." IEEE transactions on nuclear science 63.5 (2016): 2599-2606.

[56] Gravel, Paul, et al. "Spatially-variant image-based modeling of PSF deformations with application to a limited angle geometry from a dual-panel breast-PET imager." Physics in Medicine & Biology 64.22 (2019): 225015.
[57] Sajedi, S., et al. "Limited-angle TOF-PET for intraoperative surgical applications: proof of concept and first experimental data." Journal of Instrumentation 17.01 (2022): T01002.